This Dissertation

entitled

$^{14}\mathrm{N}(p,\gamma)^{15}\mathrm{O}$

typeset with NDdiss2$_\varepsilon$ v3.2017.2 (2017/05/09) on December 4, 2019 for

Bryce Alan Frentz

This LaTeX 2$_\varepsilon$ classfile conforms to the University of Notre Dame style guidelines as of Fall 2012. However it is still possible to generate a non-conformant document if the instructions in the class file documentation are not followed!

> Be sure to refer to the published Graduate School guidelines at `http://graduateschool.nd.edu` as well. Those guidelines override everything mentioned about formatting in the documentation for this NDdiss2$_\varepsilon$ class file.

This page can be disabled by specifying the "`noinfo`*" option to the class invocation.* (i.e.,`\documentclass[...,noinfo`
)

This page is *NOT* part of the dissertation/thesis. It should be disabled before making final, formal submission, but should be included in the version submitted for format check.

NDdiss2$_\varepsilon$ documentation can be found at these locations:

`http://graduateschool.nd.edu`
`https://ctan.org/pkg/nddiss`

$^{14}\mathrm{N}(p,\gamma)^{15}\mathrm{O}$

A Dissertation

Submitted to the Graduate School
of the University of Notre Dame
in Partial Fulfillment of the Requirements
for the Degree of

Doctor of Philosophy

by

Bryce Alan Frentz

Ani Aprahamian, Director

Graduate Program in Physics
Notre Dame, Indiana
December 2019

$^{14}\mathrm{N}(p,\gamma)^{15}\mathrm{O}$

Abstract

by

Bryce Alan Frentz

$^{14}\mathrm{N}(p,\gamma)^{15}\mathrm{O}$

What do you even put in an abstract for a thesis? Seems a little ridiculous...

Bananas is fruits. Tacos is sandwiches.

NEW DEDICATION NAME

To .... probably nobody

CONTENTS

FIGURES

TABLES

PREFACE

It is often said that there are few places left to be discovered or explored. That's only true on the human scale. Using a magnifying glass, microscope, telescope or any other number of devices allows us to transcend our scale.

Taken in isolation, different structures are like characters in a story. Each contributes something to the otherall shape. Sometimes one or a handful of characters will dominate the story, but it is is only when put together that they fully explain why the world behaves the way it does.

The stars twinkle their cryptic morse code and nuclear physics is one of the best keys to their cypher.

When numbers acquire the significance of language they acquire the power to do all of the things that language can do. Describe power history success failure victory defeat character grace to become fiction, drama, and poetry.

Discovering stable relationships in a seemingly unstable world.

ACKNOWLEDGMENTS

I would like to acknowledge ...

CHAPTER 1

INTRODUCTION

1.1 Overview

1.1.1 General overview

Nuclear physics data, in both the forms of theoretical predictions and experimental results, is an ever richer trove of information useful in solving many astrophysical problems. The partnership between the fields of nuclear physics and astrophysics was actually born in the early days of nuclear physics when Sir Arthur Eddington postulated that recent laboratory discoveries could explain the energy generation of the sun and stars [23]. Therefore, developments in one area naturally link to increased knowledge in the other - a scientific point and counterpoint. It follows naturally that many astrophysical phenomena are governed by nuclear physics. So it is through this study of the microscopic aspects of the universe that we also elucidate its behavior in the grandest scales imaginable.

The general goals of the field of nuclear astrophysics are as follows:

- to understand the processes by which the chemical elements were formed
- to understand the mechanism(s) responsible for the the relative abundances between the chemical elements
- to understand the energy generation during each phase of stellar evolution.

Crucially, stellar evolution is cyclic: stars are born, evolve, and ultimately die, seeding the interstellar medium with the collective material they've created over their life in order to form the building blocks for the next stellar generation. As each of the different stellar phases are guided by the underlying nuclear physics, investigations into these questions provide a rich ink between humans and our place in the cosmos.

The synthesis of the chemical elements we see began with the universe as the Big Bang created hydrogen, helium, and trace amounts of lithium [3]. Shortly after the Big Bang, the temperature and density of the Universe dropped too low for any significant nuclear fusion to occur and overcome the mass 5 and mass 8 barriers. This was the end of Big Bang Nucleosynthesis (BBN), as after

this point, the elemental abundances were nearly stable, with the only changes coming from the radioactive decay of $^3\text{He} \rightarrow t$ and $^7\text{Be} \rightarrow {}^7\text{Li}$ [19].

From this point, generations of stellar evolution created nearly all other elements, leading to the currently observed elemental abundance distribution, shown in Figure **??**. The synthesis of elements heavier than BBN products, commonly referred to as "metals," began with the formation of the first stars. Cold gas clouds, composed primarily the BBN products of hydrogen and helium (and metals in subsequent stellar generations), coalesce under their mutual gravitational attraction, converting their gravitational potential energy to heat – increasing their pressure, density, and temperature. Upon passing a critical threshold for these physical quantities, typically temperatures >1 MK, thermonuclear fusion reactions begin in the core [37]. This transition marks the "birth" of a star, having reached a point where nuclear reactions provide a sufficient heat source to balance energy losses from radiation.

1.1.2 Stellar evolution

Every star is unique and their intrinsic quantities when forming, such as mass or initial abundance distribution, prescribe the nuclear reactions that can occur throughout their lifetimes. Despite their differences, correlations emerge in studies of their observational properties , like luminosity, mass distribution, temperature, color, etc. The most evident patterns appeared when classifying stars by luminosity (or magnitude) vs temperature (or color), named the *Hertzsprung-Russel* (HR) diagram [17, 23, 37], distilling the most important relationship between stellar properties. An example HR diagram for stars in the solar neighborhood is displayed in Figure **??**. Since HR diagrams represent a snapshot of the evolutionary tack of a set of stars, the most densely populated areas of such plots are those in which individual stars necessarily spend most of their lives. Conversely, as there is a lower probability of observing a star in a short-lived phase, sparsely populated areas of HR diagrams detail such phases of stellar burning.

The vast majority of stars lie on the diagonal band stretching from the upper left (hot, bright stars) to the lower right (cool, faint stars) of the diagram. This feature is called the main sequence. These stars support themselves through core hydrogen burning – implying that stars spend most of their lives in this long period of quiescent hydrogen burning in the *pp chains* and the CNO cycles, detailed in subsequent sections. Other prominent features of typical HR diagrams are the clusters of stars in the upper quadrants (very bright stars), commonly referred to as the giant branch, the lower left quandrant (hot, faint stars), where the white dwarf stars reside, and the lower right quadrant

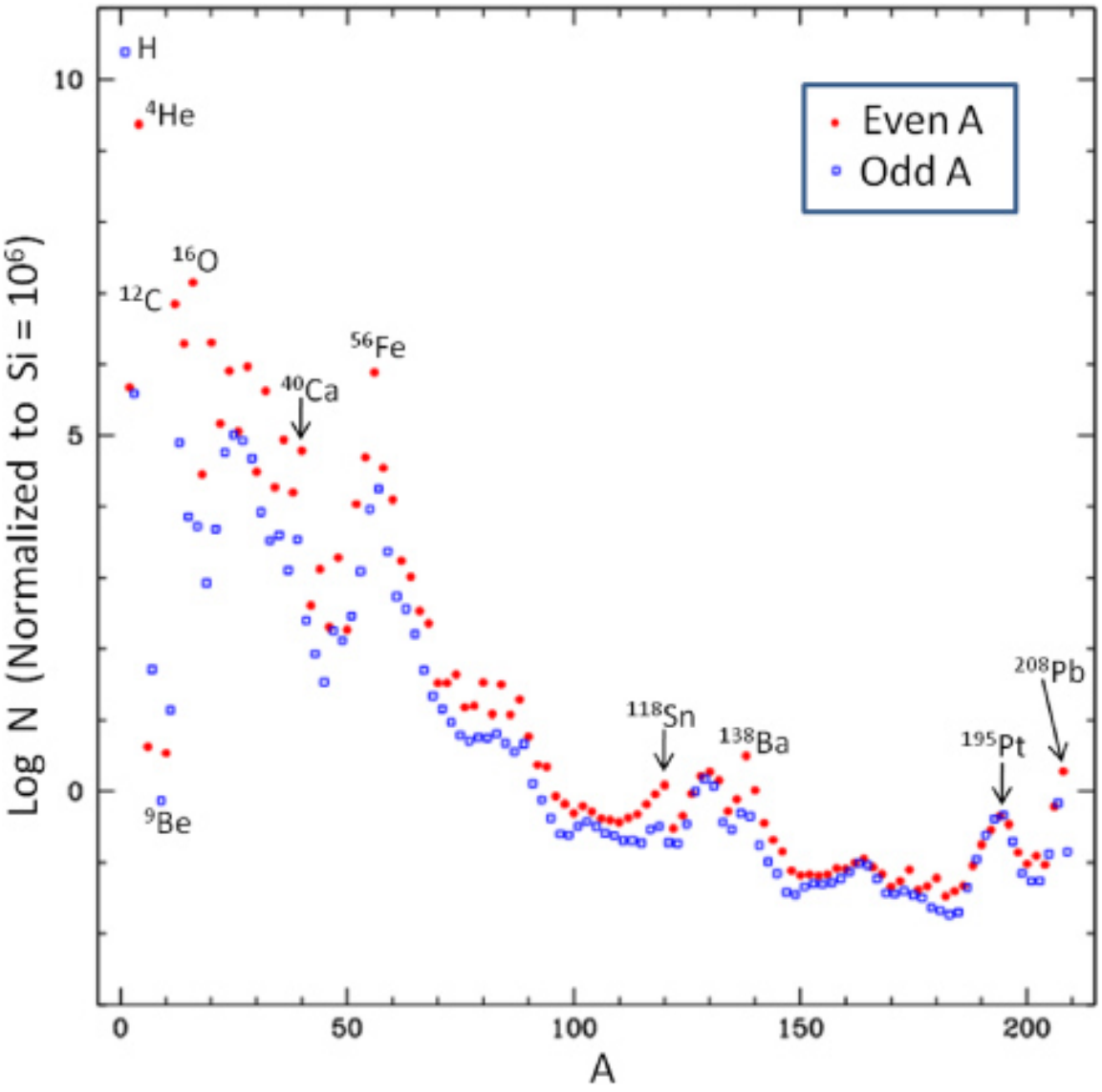

Figure 1.1. The current solar isotopic abundance pattern vs. mass number for even and odd nuclei [26]. Abundances are based on both meteoritic samples and observations of the solar photosphere.

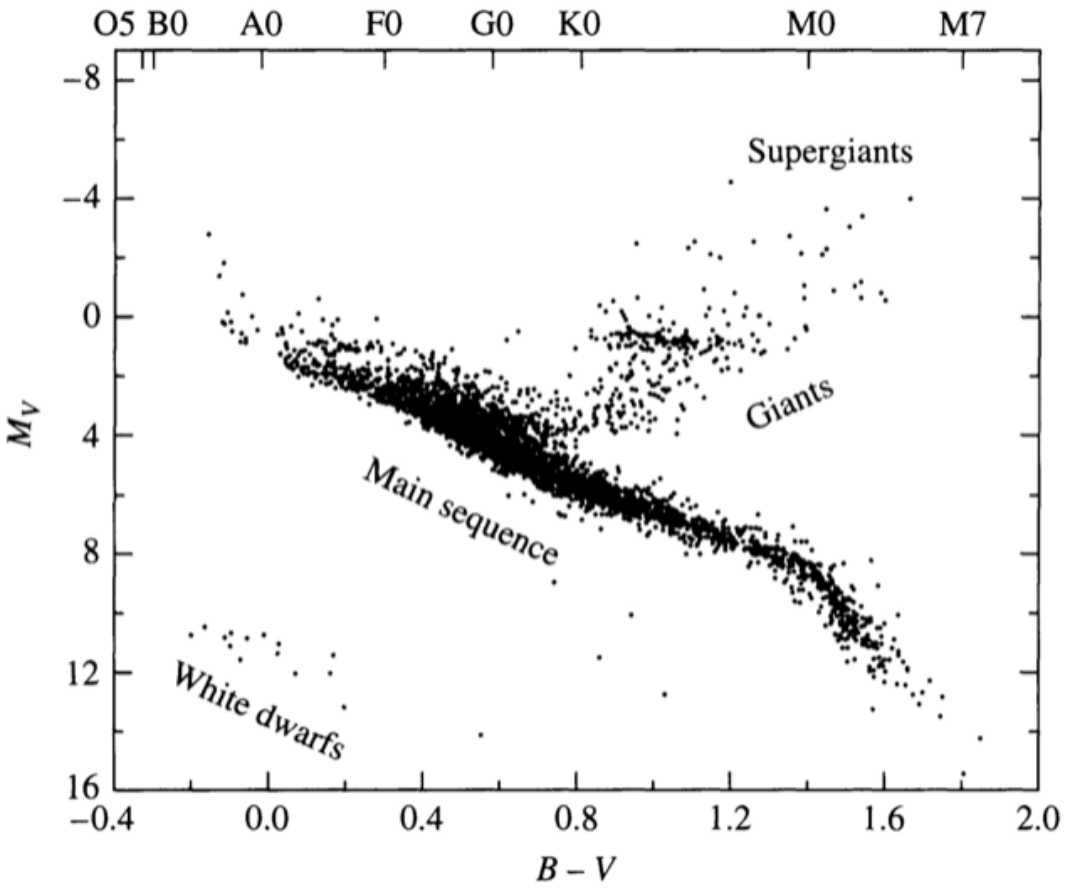

Figure 1.2. An example of a Herzprung-Russell diagram. The horizontal axis gives the temperature of the star while the vertical shows the stellar luminosities [17].

beyond the main sequence, occupied by brown dwarfs. Each classification corresponds to different nuclear reactions, with stars evolving off the main sequence being characterized by phases of burning of heavier elements, like helium or carbon.

Any single star's evolutionary track will follow different paths depending on its initial mass [23, 37]. For cosmic objects of mass $\lesssim 0.08$ $M_\odot$, where $M_\odot$ is the mass of the sun, core temperatures never rise high enough to sustain hydrogen fusion, and thus they evolve directly into brown dwarf stars. In the range of mass 0.08 $M_\odot \lesssim M \lesssim 0.4$ $M_\odot$, stars undergo core hydrogen fusion through the *pp chains*, but do not reach temperatures sufficient to initiate helium burning after exhausting hydrogen in the core. Ultimately, stars in this classification become white dwarfs. The next mass grouping consists of Sun-like stars, with masses 0.4 $M_\odot \lesssim M \lesssim 8.0$ $M_\odot$, which evolve off the main

sequence and continue growing and burning (both in the stellar core and shells in their stellar envelope). Such stars achieve temperatures high enough to create final abundance distribution composed of primarily carbon and oxygen in their core. After losing their stellar envelopes, these stars are carbon-oxygen white dwarfs. However, if such a star has a companion of sufficient mass, it will eventually explode in a type Ia supernova. Lastly, are stars of mass 8.0 $M_\odot \lesssim M$, which go through sequences of carbon, neon, oxygen, and silicon burning to produce a dominantly iron-nickel core. At this point, as the stars are more massive than the Chandrasekar limit, the gravitational attraction will exceed the support of elecron degeneracy pressure causing a core collapse (type II) supernova. Depending on the star's mass at this stage, it will become either a neutron star or black hole. While not the topic of this thesis, such explosive scenarios are currently an area of intense research as they are the location of many unresolved issues of nuclear astrophysics, including what the National Research Council identified in 2003 as one of the eleven greatest unanswered questions of the century, namely the origin of the elements heavier than iron [44].

1.1.3 Hydrogen Burning

The lifetimes of stars along the main sequence vary drastically, from millions of years to trillions of years, depending on the star's properties when forming. Likewise, the dominant type of hydrogen burning that occurs during the main sequence phase is also highly dependent on stellar characteristics like mass and initial composition. Broadly, there are two sets of nuclear processes that comprise the hydrogen burning phases in stellar cores, the *pp chains* and the CNO cycles, with each ultimately functions in a similar way, to convert four hydrogen nuclei to one helium nucleus, releasing ∼26 MeV of energy [35].

The *pp chains* are the main energy generator in smaller stars with core temperatures below 20 MK [37], like the sun. There are three variations of the *pp chains* (denoted ppI, ppII, and ppIII), shown below.

ppI	ppII	ppIII
$p\left(p, e^{+}\nu\right) d$	$p\left(p, e^{+}\nu\right) d$	$p\left(p, e^{+}\nu\right) d$
$d\left(p, \gamma\right)\,^{3}\mathrm{He}$	$d\left(p, \gamma\right)\,^{3}\mathrm{He}$	$d\left(p, \gamma\right)\,^{3}\mathrm{He}$
$^{3}\mathrm{He}\left(^{3}\mathrm{He}, 2p\right)\,^{4}\mathrm{He}$	$^{3}\mathrm{He}\left(^{4}\mathrm{He}, \gamma\right)\,^{7}\mathrm{Be}$	$^{3}\mathrm{He}\left(^{4}\mathrm{He}, \gamma\right)\,^{7}\mathrm{Be}$
	$^{7}\mathrm{Be}\left(e^{-}\nu\right)\,^{7}\mathrm{Li}$	$^{7}\mathrm{Be}\left(p, \gamma\right)\,^{8}\mathrm{B}$
	$^{7}\mathrm{Li}\left(p, \alpha\right)\,^{4}\mathrm{He}$	$^{8}\mathrm{B}\left(e^{+}\nu\right)\,^{8}\mathrm{Be}$
		$^{8}\mathrm{Be}\left(\alpha\right)\,^{4}\mathrm{He}$

Between the three branches there are clear similarities and differences. The energy released between each of ppI, ppII, and ppIII are 26.20 MeV, 25.66 MeV, and 19.75 MeV, respectively, with the difference coming from the amount of energy carried away by the electrons, positrons, and neutrinos. Of these chains, ppI is the most prominent, occurring $\sim$ 85 % of the time, where the remainder branches off as a ^{3}He nucleus will fuse with a ^{4}He nucleus, resulting in the ppII or ppIII chain, occurring $\sim$ 14.99 % and $\sim$ 0.1 % of the time, respectively [37]. Regardless of the branching for the *pp chains*, each starts with the $p\left(p, e^{+}\nu\right) d$ reaction. This reaction is governed purely by the weak interaction, and thus is about 20 orders of magnitude slower than those proceeding via the strong interaction [35], like the reactions in the chains that follow. Therefore, energy production, nucleosynthesis, and stellar evolution timescales for stars dominated by the *pp chains* are restricted by the $p\left(p, e^{+}\nu\right) d$ reaction.

However, for most stars the CNO cycles are the dominant energy source. Stellar energy generation depends sensitively on the temperature in the star's core, which is closely tied to its mass. For stars of mass $\mathrm{M} \gtrsim \mathrm{M}_{\odot}$, where cores contain carbon and oxygen seed nuclei and temperatures exceed 20 MK, the CNO cycles' energy production overtakes that of the *pp chains*. Thus, the knowledge of the overall rate of this cycle is important for the study of their evolution.

The CNO cycles are the collection of four similar energy producing cycles broadly characterized by their synthesis of helium from hydrogen with a carbon catalyst, seeded by earlier generations of stars. There are four CNO cycles, listed below with their relationships shown in Fig. **??**.

CNO1	CNO2	CNO3	CNO4
$^{12}\mathrm{C}\,(p,\gamma)\,^{13}\mathrm{N}$	$^{14}\mathrm{N}\,(p,\gamma)\,^{15}\mathrm{O}$	$^{15}\mathrm{N}\,(p,\gamma)\,^{16}\mathrm{O}$	$^{16}\mathrm{O}\,(p,\gamma)\,^{17}\mathrm{F}$
$^{13}\mathrm{N}\left(\beta^{+}\nu\right)\,^{13}\mathrm{C}$	$^{15}\mathrm{O}\left(\beta^{+}\nu\right)\,^{15}\mathrm{N}$	$^{16}\mathrm{O}\,(p,\gamma)\,^{17}\mathrm{F}$	$^{17}\mathrm{F}\left(\beta^{+}\nu\right)\,^{17}\mathrm{O}$
$^{13}\mathrm{C}\,(p,\gamma)\,^{14}\mathrm{N}$	$^{15}\mathrm{N}\,(p,\gamma)\,^{16}\mathrm{O}$	$^{17}\mathrm{F}\left(\beta^{+}\nu\right)\,^{17}\mathrm{O}$	$^{17}\mathrm{O}\,(p,\gamma)\,^{18}\mathrm{F}$
$^{14}\mathrm{N}\,(p,\gamma)\,^{15}\mathrm{O}$	$^{16}\mathrm{O}\,(p,\gamma)\,^{17}\mathrm{F}$	$^{17}\mathrm{O}\,(p,\gamma)\,^{18}\mathrm{F}$	$^{18}\mathrm{F}\left(\beta^{+}\nu\right)\,^{18}\mathrm{O}$
$^{15}\mathrm{O}\left(\beta^{+}\nu\right)\,^{15}\mathrm{N}$	$^{17}\mathrm{F}\left(\beta^{+}\nu\right)\,^{17}\mathrm{O}$	$^{18}\mathrm{F}\left(\beta^{+}\nu\right)\,^{18}\mathrm{O}$	$^{18}\mathrm{O}\,(p,\gamma)\,^{19}\mathrm{F}$
$^{15}\mathrm{N}\,(p,\alpha)\,^{12}\mathrm{C}$	$^{17}\mathrm{O}\,(p,\alpha)\,^{14}\mathrm{N}$	$^{18}\mathrm{O}\,(p,\alpha)\,^{15}\mathrm{N}$	$^{19}\mathrm{F}\,(p,\alpha)\,^{16}\mathrm{O}$

As with the *pp chains*, the net result of each of the CNO cycles is the conversion of four protons into helium, releasing $\sim$ 26 MeV of energy in the process [37]. Additionally, all of the heavier elements (carbon, nitrogen, oxygen, and fluorine) are only catalysts, with their overall abundance unchanged through the cycles while only the hydrogen is consumed. Therefore, this implies that the CNO cycles can occur even if the amount of heavy elements is relatively small, in the case of only being seeded by a single prior generation of stars [23]. Of the cycles, however, the main CNO1 cycle contributes $\sim$99% of the CNO energy production [2], so hereafter CNO1 will be referred to as simply the CNO cycle, while the others will be designated as needed.

Within the CNO cycle, the $^{14}\mathrm{N}\,(p,\gamma)\,^{15}\mathrm{O}$ reaction is the slowest and thus the rate-limiting step of the whole process, ruling the energy production and the overall time spent in this burning phase, evidenced recently by the adjustment of the estimation of globular cluster ages [24].

The relative energy production between the *pp chains* and CNO cycles are shown in Fig. **??**. It can be seen that the CNO cycle accounts for $<$1 % of solar energy production [1, 2]. However, it produces 1.6 % of solar neutrinos through the β-decay of ^{13}N and ^{15}O [9], which can be used to test assumptions of the Standard Solar Model (SSM), as these rates are one of the largest sources of uncertainty in model predictions [41]. Efforts to measure the neutrino fluxes from the β-decays of ^{13}N and ^{15}O are either ongoing or planned at the Borexino, Super-Kamiokande, and SNO+ laboratories [26].

These laboratories are well known for their contributions in solving the *solar neutrino problem* [26] (and references therein). However, after this solar problem was solved, a new problem arose, named the solar abundance problem [1, 42]. The problem is as follows, solar models describe the structure, composition, and evolution of a $1M_{\odot}$ star from ignition through the sun's current age

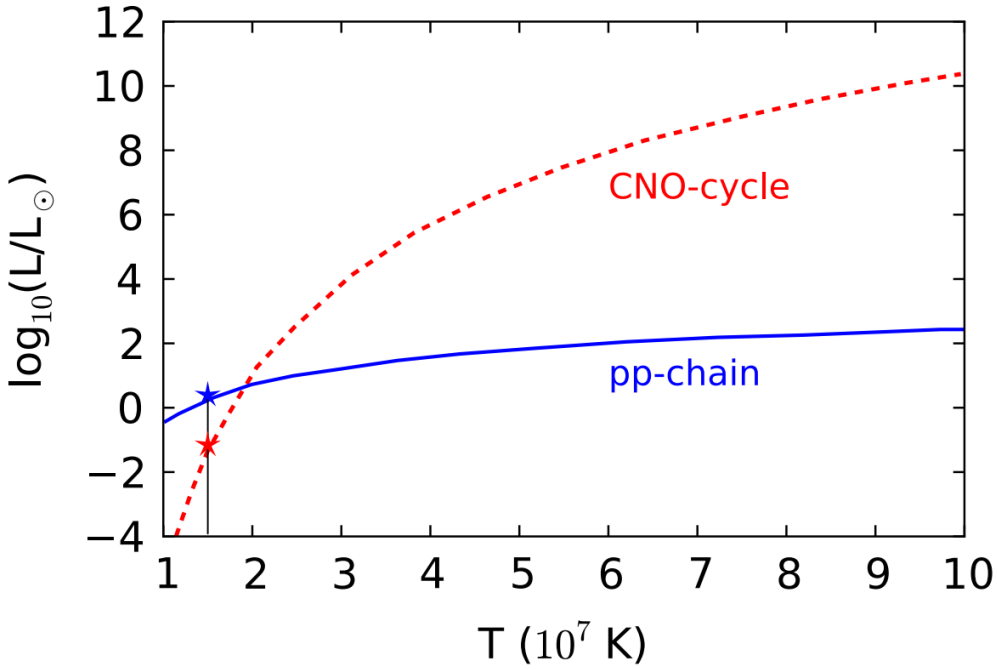

Figure 1.3. Energy dependence of the *pp chains* and the CNO cycles as a function of stellar temperature assuming a solar abundance distribution of CNO elements [15]. The sun's temperature is marked with the star in the figure. This shows that for lower mass stars like the sun the *pp chains* are the dominant mode of energy production in main sequence burning. However, for hotter, more massive stars, the CNO cycle quickly dominates.

and are constrained by the plethora of helioseismology data from the Sun. Recent analyses of the Sun's photosphere lead to a reduced metallicity estimate, destroying the agreement between helioseismology and solar models [7]. In discussing potential solutions to this problem, it was proposed to use the neutrino fluxes from the β-decay of CNO isotopes ^{13}N and ^{15}N to address this problem, as these quantities depend linearly on their abundance within the solar core [9, 10]. Therefore, with the measurement of these neutrino fluxes imminent, it is ever more important to have precise knowledge of the relevant nuclear cross-sections.

Due to the importance of the $^{14}\mathrm{N}\,(p,\gamma)\,^{15}\mathrm{O}$ reaction, it is the focus of this work. Presented first, in Sec. 1.2 and Sec. 1.3 are an overview of nuclear reactions and reaction theory relevant for nuclear astrophysics. An extension of these theories using the R-matrix formalism will be presented in Sec. 1.4. The current state of knowledge surrounding the reaction, its uncertainties, and previous

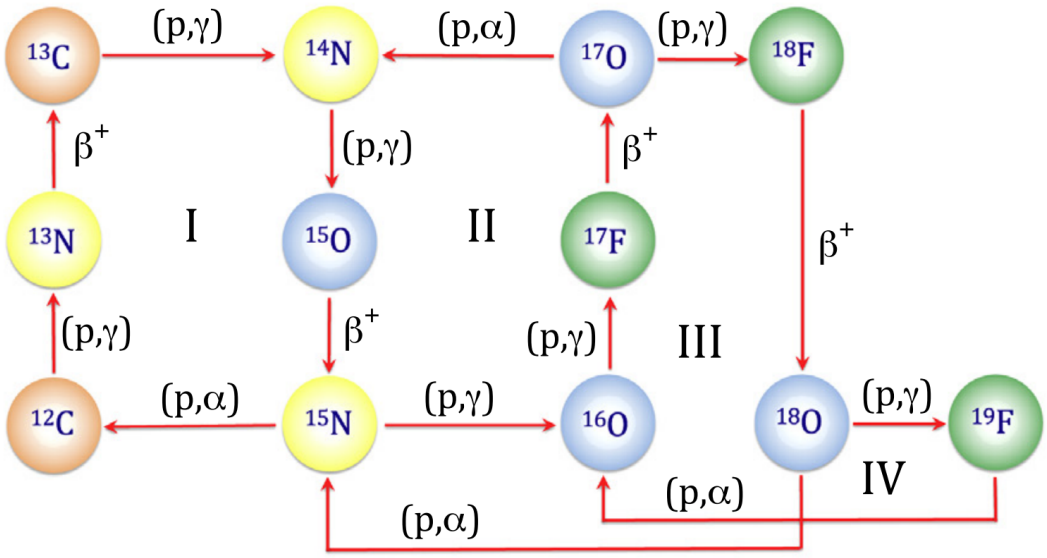

Figure 1.4. A depiction of the CNO cycles for hydrogen burning in stars [15]. Cycles II, III, and IV only contribute meaningfully at very high temperatures or explosive burning scenarios.

measurements are discussed in Sec. 1.5. After which, a summary of the Doppler Shift Attenuation Method for measuring extremely short nuclear lifetimes will be given in Sec. **??**. Finally, an outline of the remainder of this work will be presented in Sec. 1.6.

1.2 Thermonuclear reaction rates

Stars are fueled by the energy released during nuclear reactions. Recall that a nuclear reaction can be written as

$$a + A \rightarrow b + B + Q \qquad \text{or} \qquad A(a,b)B^{*} \tag{1.1}$$

where a denotes the projectile, A the target nucleus, b the ejectile, B the reaction product, and Q the energy released (or absorbed) during the reaction, typically present as kinetic energy distributed among the reaction products. For this reaction to occur, the initial nuclei must have enough energy to overcome the Coulomb repulsion created by their constituent protons. The probability of their interaction, called their cross section (σ), is therefore energy dependent. As stars are powered by

thousands of such reactions at a variety of energies, the understanding of nuclear cross-sections are crucial components to the subsequent understanding of stellar evolution and nucleosynthesis.

Consider a stellar environment filled with two types of nuclei with number densities (nuclei / cm^3) N_1 and N_2, respectively, and relative velocity v. The rate of reaction for these two species per unit volume would then be proportional to the probability that a given pair of particles would react multiplied by the number of pairs that interact per unit time. Mathematically, the reaction rate R_{12} would therefore be

$$R_{12} = \frac{N_1 N_2}{1+\delta_{12}} v\sigma(v) \tag{1.2}$$

with δ_{12} to prevent overcounting if the particles are identical. In stellar environments, the relative velocity between the two particles can take a range of values related to the temperature, T. The probability distribution of the potential relative velocities, $P(v)$, is described by the Maxwell-Boltzmann distribution [37]:

$$P(v) = 4\pi v^2 \left(\frac{\mu}{2\pi kT}\right)^{3/2} \exp\left(-\frac{\mu v^2}{2kT}\right) \tag{1.3}$$

where k is the Boltzmann constant, relating the kinetic energy of a particle to the temperature of its environment, and $\mu = m_1 m_2/(m_1+m_2)$ is the reduced mass of the two nuclei. Explicitly, the probability that a given pair of nuclei having a relative velocity between v and $v+dv$ is $P(v)dv$ and satisfies the unity expression

$$\int_0^\infty P(v)dv = 1. \tag{1.4}$$

Therefore, the reaction rate per particle pair $\langle\sigma v\rangle$ with relative velocity v is the average value of v multiplied with $\sigma(v)$ for a given temperature,

$$\langle\sigma v\rangle = \int_0^\infty vP(v)\sigma(v)dv. \tag{1.5}$$

Using a few useful substitutions, this formulation allows us to rewrite Equation 1.2, the general reaction rate, as a function of energy instead of velocity. To do this, recall that the kinetic energy is $E = \frac{1}{2}\mu v^2$ and its derivative is $dE/dv = \mu v$. By explicitly writing the Maxwell-Boltzmann

distribution into and replacing the appropriate terms in Equation 1.5 leads to

$$\langle \sigma v \rangle = \left(\frac{8}{\pi\mu}\right)^{1/2} \left(\frac{1}{kT}\right)^{3/2} \int_0^\infty \sigma(E) E \exp\left(-\frac{E}{kT}\right) dE. \tag{1.6}$$

It is important to note that the only unknown in the entirety of the reaction rate is the expression of the nuclear cross section as a function of energy, $\sigma(E)$. Therefore, to understand the reaction rates for stellar environments, $\sigma(E)$ needs to be determined.

Recall that earlier, the cross section, $\sigma(E)$, is the probability of two nuclei reacting if brought together at a specific energy, E. While this quantity is an expression of the probability of reaction, it is analogous to the classical, cross-sectional area of the nucleus, so it is expressed in units of area (specifically barns, where 1 b = 10^{-24}cm^2). An insightful description is to think of the cross section coming from throwing two balls at each other with random perturbations off of a common axis, classically. If either ball's size changes (cross-sectional area), the chances of hitting will also change in a manner that is directly proportional to the alteration of the respective sizes of the balls since the total cross-sectional area is $\sigma = \pi(R_1 + R_2)^2$. For our quantum mechanical nuclei, the nuclear size needs to be replaced with the deBroglie wavelength, resulting in $\sigma = \pi\lambda$. Translating this into another formulation that is more familiar, the cross section is the number of reactions occurring divided by the number of potential reactions, given as

$$\sigma = \frac{N_R}{(N_i N_t)/A}, \tag{1.7}$$

where N_R is the number of reactions that take place per unit time, N_i is the number of incident nuclei per unit time, N_t is the number of target nuclei within the area of incidence, A.

In astrophysical environments, nuclei typically do not have enough energy to overcome the Coulomb repulsion provided by the protons within the nucleus and combine with the attractive nuclear strong force. A diagram of the combined nuclear and Coulomb potentials is given in Fig. **??**. The repulsive Coulomb interaction causes the cross section to drop quickly at low center-of-mass energies [23]. Thus, for such reactions to occur, nuclei must actually tunnel through the Coulomb barrier.

The Coulomb penetrability, P, can be approximated as the leading term of the s-wave ($\ell = 0$) barrier transmission coefficient:

$$P = \exp(-2\pi\eta), \tag{1.8}$$

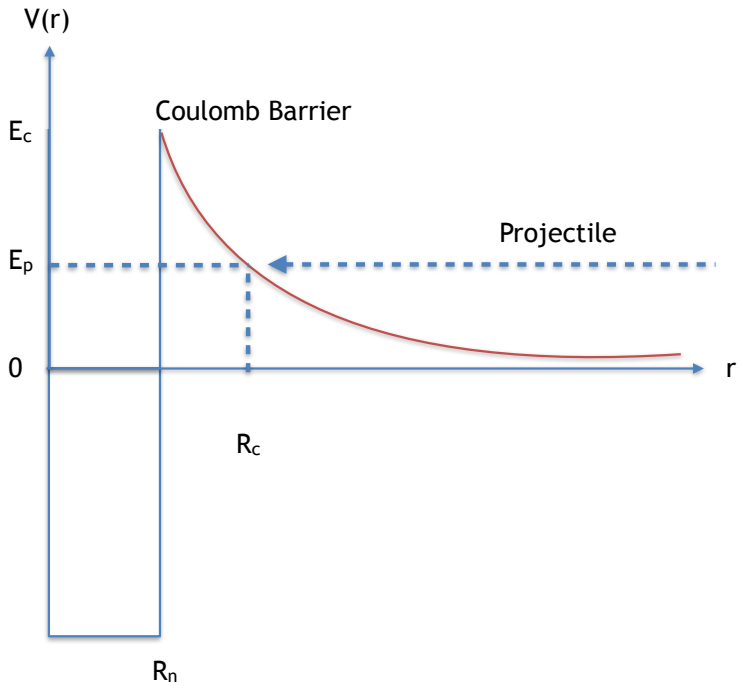

Figure 1.5. Schematic plot of the combined attractive nuclear and repulsive Coulomb potentials where R_n is the nuclear radius, R_c is the classical turning point due to Coulomb repulsion, E_c is the height of the Coulomb barrier, and E_p is the projectile's energy. Because this is a quantum system, the projectile has a chance to tunnel through the Coulomb barrier and make it into the attractive nuclear potential when it has energy $E_p < E_c$.

where η is the Sommerfeld parameter,

$$\eta = \frac{Z_1 Z_2 e^2}{4\pi\epsilon_0 \hbar v} = \alpha Z_1 Z_2 \sqrt{\frac{\mu c^2}{2E_{cm}}}, \tag{1.9}$$

where Z_i is the respective proton number of each nucleus, v is the incident center-of-mass velocity, $\alpha \approx 1/137$ is the fine-structure constant, μ is the reduced mass of the system, and E_{cm} is the center of mass energy of the interacting nuclei. Numerically, it is convenient to evaluate the quantity $2\pi\eta$, known as the Gamow factor, as

$$2\pi\eta = 0.989534 Z_1 Z_2 \left(\frac{\mu}{E_{cm}}\right)^{1/2}, \tag{1.10}$$

where E_{cm} is expressed in units of MeV and μ in atomic mass units (amu or simply, u).

By factoring the Coulomb penetrability out of the cross section, we can separate the contributions from the Coulomb barrier to isolate the nuclear physics in the astrophysical S-factor, $S(E)$,

$$\sigma(E) = \frac{1}{E} S(E) e^{-2\pi\eta}. \tag{1.11}$$

The astrophysical S-factor is slowly varying with energy, unlike the nuclear cross section. Fig. **??** provides a comparison of the energy dependence of both the cross section and S-factor, where you can see that the cross section drops by orders of magnitude in an energy regime where the S-factor is relatively constant. This implies that the Coulomb effects can obscure important nuclear physics effects. Additionally, as the S-factor is slowly varying, extrapolations of it's behavior towards zero energy from higher energy data are significantly more reliable than those made from cross section data.

Now, after defining the S-factor, the reaction rate can be written finally as

$$\langle \sigma v \rangle = \left(\frac{8}{\pi\mu}\right)^{1/2} \left(\frac{1}{kT}\right)^{3/2} \int_0^\infty S(E) \exp\left(-\frac{E}{kT} - \frac{b}{E^{1/2}}\right) dE. \tag{1.12}$$

where b has units of $(\text{MeV})^{1/2}$ and is given as

$$b = 0.989534 Z_1 Z_2 \mu^{1/2}. \tag{1.13}$$

Recall that one of the most useful features of $S(E)$ is that it is typically smoothly varying with respect to energy, meaning that the reaction rate in total is dependent primarily on the exponential term inside the integrand of Eq. 1.12. The two components of this term arise from the Coulomb

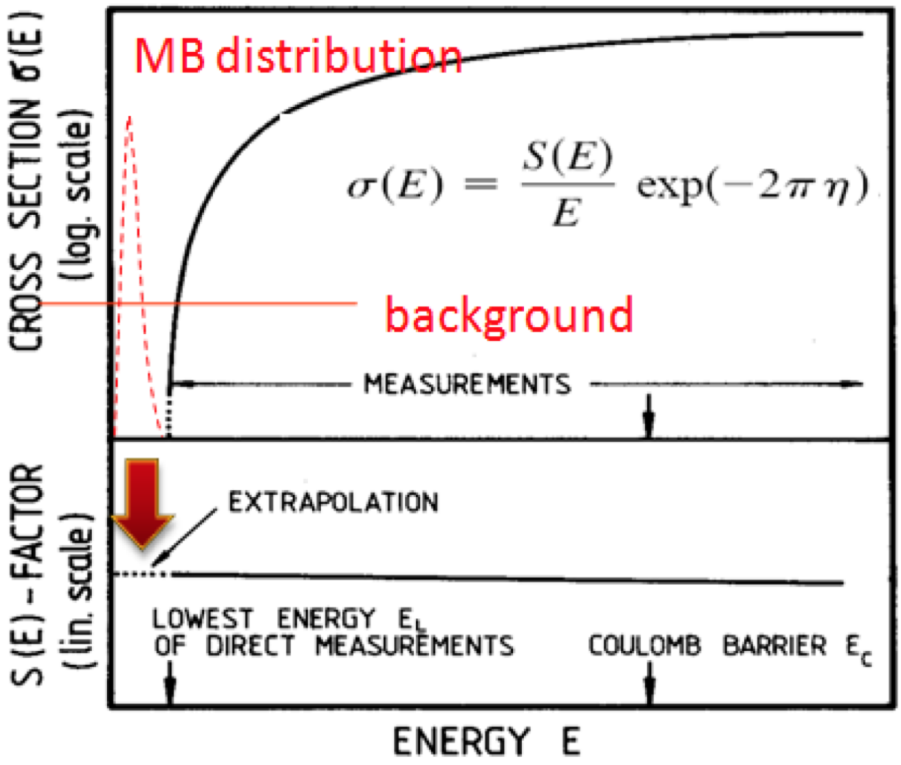

Figure 1.6. The energy dependence of the nuclear cross section and astrophysical S-factor [35]. The cross section drops dramatically due to Coulomb repulsion as the incident energy drops, however the S-factor, by removing the Coulomb penetrability varies slowly towards the Gamow window (barring the absence of nuclear resonances).

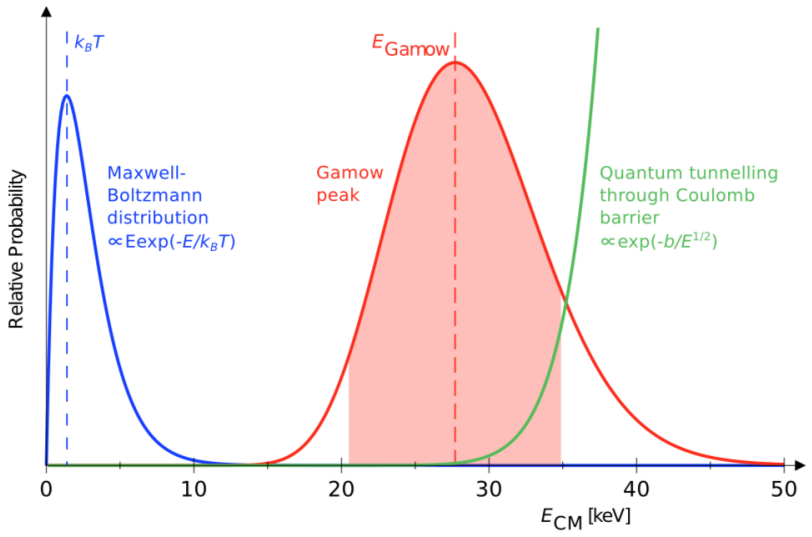

Figure 1.7. The two dominant terms of the reaction rate calculation and their convolution (Gamow peak) for the $^{14}\mathrm{N}(p,\gamma)^{15}\mathrm{O}$ reaction at $T = 0.016$ GK [11]. The y-axis is given in arbitrary units.

penetrability and the Maxwell-Boltzmann velocity distribution described in Eq. 1.3. The convolution of these two quantities can be used to estimate the energy range where the reaction rate should be maximized for given stellar temperatures [23].

The Coulomb penetrability and Maxwell-Boltzmann velocity distribution have opposite behaviors in energy regimes with the penetrability dropping to zero at low energies while the probability distribution for the velocities is maximized at low energies and vice-versa at high energies. The product of the terms is therefore negligible for nearly all energies. However, for a small set of energies this product, and therefore the reaction rate, maximizes. This behavior, as well as their product, commonly called the Gamow Peak, is presented in Fig. **??**.

The Gamow peak's maximum can be obtained with basic calculus on the exponential term in Eq. 1.12 by setting the derivative with respect to energy equal to zero and solving for the energy value. This results in the maximum energy of the reaction rate being

$$E_0 = \left(\frac{bkT}{2}\right)^{2/3}. \tag{1.14}$$

For a given stellar temperature, T, the average effective energy at which the reaction occurs is E_0. Additionally, this also allows for an approximation of the range of energies over which the reaction

primarily occurs, provided that the S-factor is smoothly varying (which is not true if resonances are present, which will be discussed in the next section). This range of energies is known as the Gamow Window, Δ:

$$\Delta = \frac{4}{\sqrt{3}}\sqrt{E_0 kT}. \tag{1.15}$$

The Gamow window identifies the range of energies over which experimental data should be taken to provide a complete understanding of stellar processes and the interplay of the Maxwell-Boltzmann velocity distribution with the Coulomb penetrability to create the Gamow window is presented in Fig. **??**. As an example, the $^{14}\mathrm{N}\,(p,\gamma)\,^{15}\mathrm{O}$ reaction in the sun has a Gamow peak energy at $E_0 = 26.6$ keV and $\Delta = 13.6$ keV, meaning that measuring the cross section in the energy range of 19.8 - 33.4 keV is crucial in the understanding of this reaction.

Unfortunately, though, measuring at energies this low is not feasible, experimentally. This is because at these energies the signal-to-noise ratio of observables drops dramatically and the signals of interest are obscured within background noise. To provide accurate measurements of such situations, experiments must necessarily then occur in the timescale of years to measure a single datum. This is simply unfeasible, practically, and our understanding must rely on extrapolations from higher-energy data. As the $^{14}\mathrm{N}\,(p,\gamma)\,^{15}\mathrm{O}$ reaction is not alone in having a Gamow window at such low energies, extrapolation techniques must be employed to describe the cross section and S-factor for nearly all astrophysically important reactions at the Gamow window. This, then, in a nutshell highlights the primary goal of experimental nuclear astrophysics: to a) directly measure relevant cross-sections down to astrophysical energies when possible, or b) measure as low in energy as possible to provide the best constraint for theoretical extrapolations to Gamow energies.

1.3 Nuclear reactions

For the $^{14}\mathrm{N}\,(p,\gamma)\,^{15}\mathrm{O}$ reaction, both resonant and direct capture contributions are important. Resonant reactions are those in which an incoming particle combines with a target to form an excited state in a compound nucleus and then subsequently decay as part of a two-step process. Alternatively, direct capture reactions are those in which the particle pair proceeds directly to a final, bound nuclear state in one step. An energy level diagram of the $^{14}\mathrm{N}\,(p,\gamma)\,^{15}\mathrm{O}$ reaction is shown in Fig. **??**.

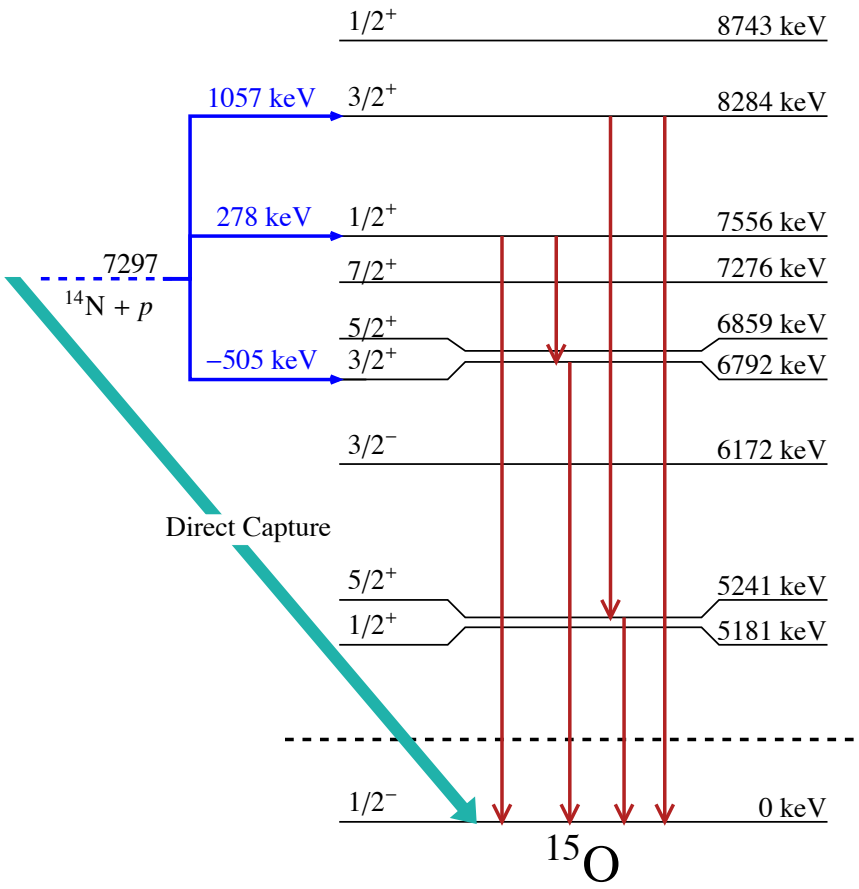

Figure 1.8. An energy level diagram of the $^{14}\mathrm{N}\,(p,\gamma)\,^{15}\mathrm{O}$ reaction. This shows the pathways of decay to the ground state of the $^{15}\mathrm{O}$ nucleus. The paths shown in red indicate a resonance reaction, with the formation of the compound nucleus in an excited state, while the path in green shows a direct capture process, proceeding immediately to the final state (ground in this example) from any energy above the proton threshold.

1.3.1 Direct capture reactions

The other side of the proverbial coin from resonant reactions is direct capture, or nonresonant reactions. Such cases are defined as those in which the cross section and S-factor vary smoothly with energy, being the result of a one-step, electromagnetic process where the capture proceeds from the initial state of two incident particles to the final, bound state of the system. This is process is also highlighted as a part of Fig. **??**.

With nonresonant reactions, the S-factor varies smoothly with energy. This means that the earlier characterization of the S-factor, reaction rate, and Gamow energy/window parameters in Equations 1.6 - 1.15 are applicable for the case of direct reactions. In extrapolating experimental data to stellar energy ranges, it is often useful to express an effective S-factor, S_{eff} from the Taylor expansion of the component functions [23],

$$S_{\text{eff}} = S(0)\left(1 + \frac{5kT}{36E_0}\right) + S'(0)E_0\left(1 + \frac{35kT}{36E_0}\right) + \frac{1}{2}S''(0)E_0^2\left(1 + \frac{89kT}{36E_0}\right), \tag{1.16}$$

where E_0 is the Gamow peak energy from Equation 1.14. Armed with this expansion, the S-factor can be successfully extrapolated to low, stellar energies in cases where the S-factor varies slowly with energy. This means that for nonresonant reactions, $S(E)$ can be approximated by its zero-energy value, $S(0)$, and only small corrections given by its first and second derivatives, $S'(0)$ and $S''(0)$, respectively.

1.3.2 Resonant reactions

The presence of a resonance enhances the cross section at its specific center-of-mass energy and means that the S-factor no longer varies smoothly with respect to energy. The specific increase is highly dependent on the situation since, as a two-step process, it depends on the probability of both forming the compound nucleus and decaying via a specific pathway, also shown in Fig. **??**. To understand this mathematically, consider an isolated, narrow resonance at energy E_R; the reaction cross section under the influence of such a resonance is described by the Breit-Wigner formula:

$$\sigma_{BW}(E) = \pi\lambda\!\!\!^{-2}\frac{2J_R + 1}{(2J_1 + 1)(2J_2 + 1)}\frac{\Gamma_{\text{in}}\Gamma_{\text{out}}}{(E - E_R)^2 + \Gamma_T^2/4} \tag{1.17}$$

where $\lambda\!\!\!^{-}$ is the deBroglie wavelength corresponding to the incident momentum, $p = \hbar/\lambda\!\!\!^{-}$, J_1 and J_2 are the spins of the target and projectile, J_R is the spin of the resonance in the compound nucleus, Γ_{in} and Γ_{out} are the entrance and exit reaction channel widths (essentially the probability

for a particular part of the process to occur), and Γ_T is the total width ($\Gamma_t = \Gamma_1 + \Gamma_2 + ...\Gamma_n$). The total width is related to the mean lifetime, τ, of the excited state by

$$\tau\Gamma_T = \hbar. \tag{1.18}$$

For most nuclear states, the widths can be determined experimentally, allowing for the understanding of the total width, Γ_T. However, due to many of the earlier described constraints, this is not always easy in practice. Additionally, the fact that different resonances have different strengths and can potentially dominate the contributions of others adds another complication. On the other hand, this implies that the total width will be dominated by that specific decay's width. If the dominant decay is one of the primary entrance or exit channels astrophysically, this will have a proportionally large effect on the overall cross section and reaction rate. In the case of the $^{14}\mathrm{N}\,(p,\gamma)\,^{15}\mathrm{O}$ reaction, there are two states near the proton threshold, one above and one below in energy, as shown in Fig. **??**, and these two provide the largest contributions to the overall astrophysical reaction rate.

To characterize this, we replace the Breit-Wigner formula from Equation 1.17 into the reaction rate equation 1.6 [23]. This leads to

$$\langle\sigma v\rangle_{\mathrm{BW}} = \left(\frac{8}{\pi\mu}\right)^{1/2}\left(\frac{1}{kT}\right)^{3/2}\int_0^\infty \sigma_{\mathrm{BW}}(E)E\exp\left(-\frac{E}{kT}\right)dE. \tag{1.19}$$

Because we are considering a narrow energy range for this resonance, both the energy, E, and the exponential term provided by the Maxwell-Boltzmann velocity distribution, $\exp\left(-E/kT\right)$, are constant over the integration. This allows us to rewrite the integral as

$$\langle\sigma v\rangle_{\mathrm{BW}} = \left(\frac{8}{\pi\mu}\right)^{1/2}\left(\frac{1}{kT}\right)^{3/2}E_R\exp\left(-\frac{E_R}{kT}\right)\int_0^\infty \sigma_{\mathrm{BW}}(E)dE. \tag{1.20}$$

The previous integral is proportional to the area under the resonance cross section and is known as the resonance strength. By substituting the Breit-Wigner formula, the integral becomes

$$\int_0^\infty \sigma_{\mathrm{BW}}(E)dE = \pi\lambda\!\!\!^{-2}_R\left(\frac{2J_R+1}{(2J_1+1)(2J_2+1)}\right)(1+\delta_{12})\Gamma_{\mathrm{in}}\Gamma_{\mathrm{out}}\int_0^\infty \frac{1}{(E-E_R)^2+(\Gamma_T/2)^2}dE, \tag{1.21}$$

which is solved analytically as

$$\int_0^\infty \sigma_{\mathrm{BW}}(E)dE = \pi\lambda\!\!\!^{-2}_R\left(\frac{2J_R+1}{(2J_1+1)(2J_2+1)}\right)(1+\delta_{12})\frac{\Gamma_{\mathrm{in}}\Gamma_{\mathrm{out}}}{\Gamma_T}. \tag{1.22}$$

For simplicity, the statistical factor, ω, is now defined as

$$\omega = \frac{2J_R + 1}{(2J_1 + 1)(2J_2 + 1)}(1 + \delta_{12}) \tag{1.23}$$

and the width ratio, γ, is

$$\gamma = \frac{\Gamma_{\text{in}}\Gamma_{\text{out}}}{\Gamma_T}, \tag{1.24}$$

leading to

$$\int_0^\infty \sigma_{\text{BW}}(E)dE = 2\pi^2 \lambda\!\!\!^{-2}_R \omega\gamma. \tag{1.25}$$

The product $\omega\gamma$ is called the resonance strength and is very important for reaction rate calculation, since the rate is dependent primarily on it and the resonance energy, E_R. This can be seen by implementing this integral calculation with the earlier derivation in Equation 1.19, resulting in

$$\langle \sigma v \rangle = \left(\frac{2\pi}{\mu kT}\right)^{3/2} (\omega\gamma)\hbar^2 \exp\left(-\frac{E_R}{kT}\right). \tag{1.26}$$

1.4 R-matrix theory

In many cases, the nuclear cross-section landscape is quite complicated, with the combined effects of multiple resonances and direct capture contributions. With all of this overlap, the Breit-Wigner formulation starting in Equation 1.17 is no longer valid. Therefore, a reliable theory accounting for all contributions and interferences is needed to describe relevant information and perform meaningful extrapolations. For these purposes, R-matrix theory was developed and is now commonly used in nuclear astrophysics calculations; details of its formal derivation can be found in References [8, 27].

The core concept of R-matrix theory is to describe the wave function of the system by matching individual components in the region of the compound nucleus where the nuclear potential present to an exterior region in which only the Coulomb potential contributes and nucleons are treated as individual particles. At the boundary of these two regions, also known as the channel radius a_c, the wave functions and their derivatives must match. The R-matrix actually relates these wave functions for each different reaction channel and is defined as

$$\mathbf{R}_{c'c} = \sum_\lambda \frac{\gamma_{\lambda c'}\gamma_{\lambda c}}{E_\lambda - E}, \tag{1.27}$$

where c and c' are the respective entrance and exit channels of the given reaction and the γ_λ is the reduced width, given as

$$\gamma_\lambda^2 = \hbar^2/(2ma_c)u_\lambda^2(a_c), \tag{1.28}$$

with the u_λ forming a complete set of basis states that satisfy the Schrödinger equation.

While the theory is named for the R-matrix, the cross section is actually calculated through other intermediate quantities, namely the collision matrix, $\mathbf{U}$, and the transition matrix, $\mathbf{T}$. The collision matrix relates specifically the incoming channels, y_c, to those of the outgoing particles, x_c, defined as

$$x_c = -\sum_{c'} \mathbf{U}_{c'c} y_{c'}. \tag{1.29}$$

Ultimately, $\mathbf{U}$ is proportional to the R-matrix as

$$\mathbf{U} \propto |\mathbf{R}|^2. \tag{1.30}$$

The transition matrix, on the other hand, is defined through the collision matrix as

$$\mathbf{T}_{c'c} = e^{2\imath\omega_c}\delta_{c'c} - \mathbf{U}_{c'c}, \tag{1.31}$$

, where ω_c represents the Coulomb phase shift and $\delta_{c'c}$ is the Dirac delta function relating channels c' and c. The angle integrated cross section is then

$$\sigma_{\alpha'\alpha} = \frac{\pi}{k_\alpha^2} \sum_{J\ell'\ell s's} \omega |\mathbf{T}^J_{c'c}|^2 \tag{1.32}$$

where the α's identify the interacting particle pair, the ℓ's are the respective orbital angular momenta of the particles, the s's are their respective spins, J is the total angular momentum of the system, and ω is the statistical spin factor as defined by Equation 1.23.

In this work, the multichannel, multilevel R-matrix code AZURE [8] was used to perform the calculations. A user inputs the spin-parity of the nuclear states, initial energies, partial widths of the excited states, the ANCs of bound states, and any external cross section or S-factor data into AZURE. The computation of S-factor and cross section are done via a simple GUI interface. The results are truncated to finite eigenstates behind the scenes to allow the code to operate quickly. As such, a background pole is typically included at high-energy to account for contributions from

states not included in the calculations. The theory is also referred to as phenomenological R-matrix because each of the γ_λ's and E_λ's in Equation 1.27 are free fit parameters.

1.5 The $^{14}N(p,\gamma)^{15}O$ reaction

The $^{14}N(p,\gamma)^{15}O$ reaction has been investigated many times in recent years by a wave of campaigns spurred by new facilities, equipment, and analyses [12–14, 18, 20, 21, 24, 25, 28–33, 36, 39, 40, 43, 45, 46]. Collectively, these experiments represent an effort to understand the astrophysical S-factor at stellar energies through both direct and indirect methods. The indirect approaches have two faces: measuring the width of the subthreshold state at excitation energy $E_x = 6792$ keV (E_R = -505 keV) and the Asymptotic Normalization Coefficient (ANC) of the ground state, while the direct approach is simply that - measuring the cross section to low energies and extrapolating from that data to astrophysical energies, usually with the help of theories like R-matrix. The level scheme of the reaction product of ^{15}O is shown in Fig. **??**.

1.5.1 Reaction cross section

Cross section measurements of the $^{14}N(p,\gamma)^{15}O$ reaction have been made and the contributions of the different γ-ray transitions have been disentangled to characterize the behavior of the S-factor and provide more reliable low-energy extrapolations. Measurements have ranged as low in energy as 70 keV (center-of-mass), still far above the solar Gamow window at 27 keV. Five different capture transitions contribute to the cross section at low energies: those proceeding through the DC/R→gs (Direct capture or resonant capture to the ground state), the DC/R→6.79 MeV primary transition, the DC/R→6.17 MeV primary transition, the DC/R→5.24 MeV primary transition, and the DC/R→5.18 MeV primary transition. In evaluating the total S-factor, each of these transitions contributes and must therefore be known in turn.

The first comprehensive measurement of the $^{14}N(p,\gamma)^{15}O$ reaction was performed by Schröder *et al.* in 1987 [39]. They studied the reaction with protons ranging in energy from 0.2 - 3.6 MeV and found that the DC/R→gs transition accounted for near 50 % of the total S-factor when extrapolated to zero energy, which itself was determined to be $S(0) = 3.2 \pm 0.54$ keV b. The dominant uncertainty the authors found was caused by the interference of the subthreshold state at 6.79 MeV (505 keV below the proton threshold) with the ground state capture, assigning the state a width of $\Gamma^{6.79} =$ 6.3 eV. These results were then used in further reviews [2] and the NACRE tabulations of reaction rate data [5].

In 2001, however, Angulo *et al.* revisited the data from Schröder *et al.* [39] using the R-matrix formalism and recommended an $S(0)$ value lower by nearly a factor of two [4]. This owed primarily to two discoveries in the analysis: a new value for the contribution from the ground state capture, revising it to $S_{gs}(0) = 0.08$ keV b, and the dominance that the width of the 6.79 MeV level shows on the behavior of $S(0)$. Consequently, they recommended new values for the total S-factor of $S(0) = 1.77 \pm 0.20$ keV b and a gamma width of $\Gamma^{6.79}$=1.75 eV, nearly a factor of four change. The authors also identified the contribution of the DC/R→6.17 MeV primary transition to be the other important transition, with all others accounting for $< 5\%$ of the total astrophysical S-factor. This study, similar to its subject reaction, set off a chain of new measurements and re-analyses of data with R-matrix techniques. The vast majority of these studies were done by the groups at TUNL and LUNA, with the results of all studies tabulated in Table **??**.

The most recent measurements were published by Li *et al.* in 2016 [29] and Wagner *et al.* in 2018 [45]. These experiments differed in their aim. The Li experiment focused on higher-energy contributions and determined radiative capture data for capture to the 6.79 MeV level in the 1.5- to 3.4-MeV proton energy range and the proton energy range of 0.6 - 3.4 MeV for the DC/R→gs transition from 0.6 to 3.4 MeV. The authors also reported angular distributions for their measurements. The authors identified the primary, remaining sources of uncertainty as the DC/R→gs primary transition, the DC/R→6.17 MeV level primary transition, and the Γ width of the 6.79 MeV state. Fig. **??** shows the effects of these uncertainties in the authors' R-matrix calculations and how it differs from other calculations. Due to the astrophysical importance of this reaction detailed in Section 1.1, an accurate determination of this extrapolated S-factor is of the utmost importance. Critically, the data reported do not overlap with the low energy measurements of the LUNA and TUNL groups and their absolute scale does not align, also leading to further inconsistent extrapolation and significant error in the deduced $S(0)$ value.

The Wagner *et al.* study attempted to remedy this, providing an independent cross check of the ground state and 6.79 MeV capture transitions in the proton energy range of E_p = 366–1289 keV, overlapping with the low-energy data sets. In the study, the authors found S-factors elevated significantly above those of any previous measurement for both of the transitions measured. Due to this, their results for the extrapolated $S(0)$ and contributions from the DC/R→6.79 MeV transition agree with those from Li *et al.*, but they are unable to draw conclusions about the ground state transition or any of the other, weaker transitions. Ultimately, this means that their results were unable to address any of the major uncertainties left plaguing the situation.

		Astrophysical S-factor $S(0)$ (keV b)				
Year	Reference	R/DC $\rightarrow$ 0.00	R/DC $\rightarrow$ 6.79	R/DC $\rightarrow$ 6.17	Others[d]	Total
1987	Schröder *et al.* [39]	1.55 ± 0.34	1.41 ± 0.02	0.14 ± 0.05	0.1	3.20 ± 0.54
2001	Angulo *et al.*[a] [4]	$0.08^{+0.13}_{-0.06}$	1.63 ± 0.17	$0.06^{+0.01}_{-0.02}$	$--$	1.77 ± 0.20
2003	Mukhamedzhanov *et al.* [34]	0.15 ± 0.07	1.40 ± 0.20	0.133 ± 0.02	0.02	1.70 ± 0.22
2004	Formicola *et al.* [20]	0.25 ± 0.06	1.35 ± 0.05 (stat) ± 0.08 (sys)	$0.06^{+0.01b}_{-0.02}$	0.04	1.7 ± 0.1 (stat) ± 0.02 (sys)
2005	Imbriani *et al.* [25]	0.25 ± 0.06	1.21 ± 0.05	0.08 ± 0.03	0.07	1.61 ± 0.08
2005	Runkle *et al.* [36]	0.49 ± 0.08	1.15 ± 0.05	0.04 ± 0.01	$--$	1.68 ± 0.09
2005	Angulo *et al.* [6]	0.25 ± 0.08	1.35 ± 0.04	0.06 ± 0.02	0.04	1.70 ± 0.07 (stat) ± 0.10 (sys)
2006	Bemmerer *et al.* [12]	$--$	$--$	$--$	$--$	1.74 ± 0.14 (stat) ± 0.14 (sys)[c]
2008	Marta *et al.* [30]	0.20 ± 0.05	$--$	0.09 ± 0.07	$--$	1.57 ± 0.13
2010	Azuma *et al.* [8]	0.28	1.3	0.12	0.11	1.81
2011	Adelberger *et al.* [1]	0.27 ± 0.05	1.18 ± 0.05	0.13 ± 0.06	0.08	1.66 ± 0.08
2016	Li *et al.* [29]	0.42 ± 0.04 (stat) $^{+0.09}_{-0.19}$(sys)	1.29 ± 0.06 (stat) ± 0.06 (sys)	$--$	$--$	$--$
2018	Wagner *et al.* [45]	0.19 ± 0.01 (stat) ± 0.05 (sys)	1.24 ± 0.02 (stat) ± 0.11 (sys)	$--$	$--$	$--$

Table 1.1: A summary of previous S-factor determinations. a) R-matrix analysis on available data, not a measurement. b) Adopted from Angulo *et al.* [4]. c) Measured S-factor at 70 keV. d) Calculated difference of the total $S(0)$ from the other transitions.

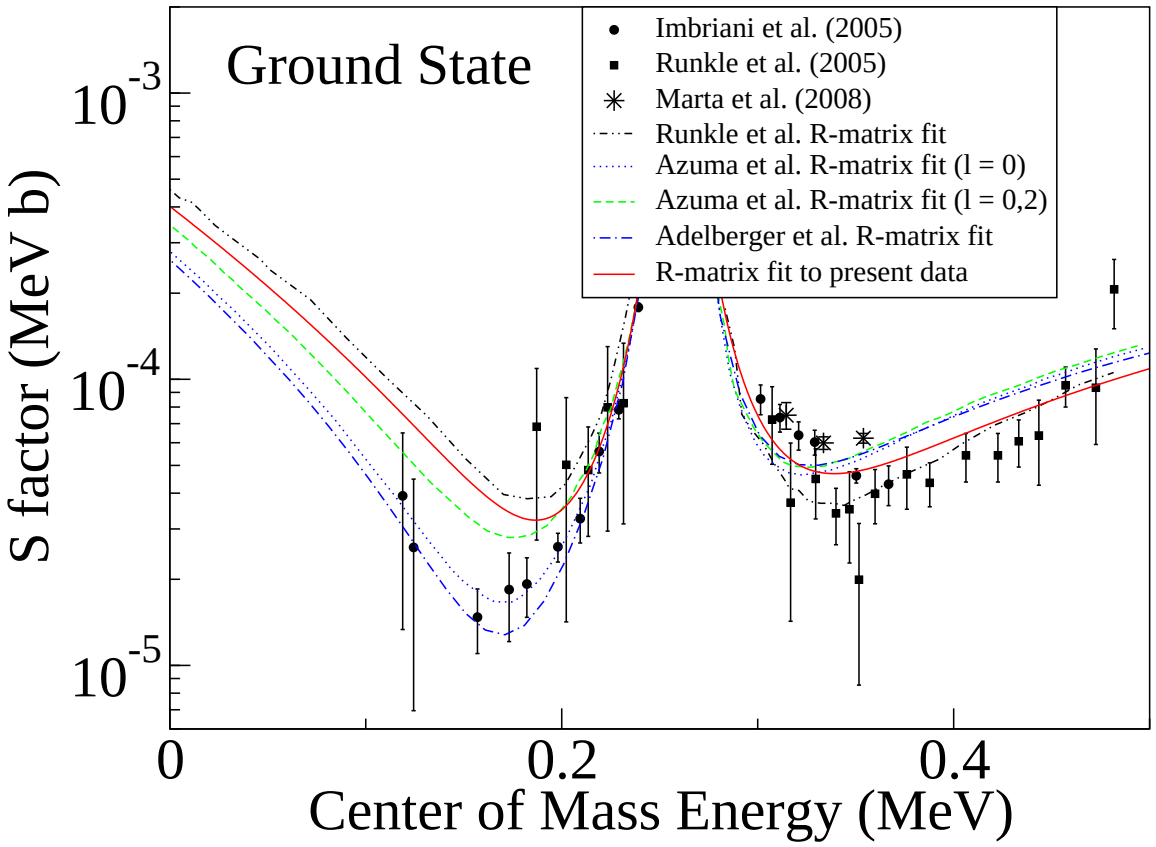

Figure 1.9. R-matrix extrapolation of the S-factor given in [29]. The authors identified the major sources of uncertainty as the uncertainty as the DC/R→gs primary transition, the DC/R→6.17 MeV level primary transition, and the Γ width of the 6.79 MeV state. Of these, the latter is the dominant term. This figure highlights the effects that these uncertainties have on low-energy extrapolations, varying by nearly a factor of two.

	$\tau_{6.79}$ fs	$\tau_{6.17}$ fs	$\tau_{5.18}$ fs	$\Gamma^{6.79}$ (eV)
Gill *et al.* [22]	< 28	< 2.5	8.2 ± 1.0	$--$
Schröder *et al.* [39]	$--$	$--$	$--$	6.3
Bertone *et al.*[a] [13]	$1.60^{+0.75}_{-0.72}$	$2.10^{+1.33}_{-1.32}$	$9.67^{+1.34}_{1.24}$	$0.41^{+0.34b}_{-0.13}$
Angulo *et al.* [4]	$--$	$--$	$--$	1.75 ± 0.60^{c}
Yamada *et al.* [46]	$0.69^{+1.10}_{-0.69}$	$--$	$--$	$0.95^{+0.60}_{-0.95}$
Formicola *et al.* [20]	$--$	$--$	$--$	0.8 ± 0.4^{c}
Schürmann *et al.* [40]	< 0.77	< 0.77	8.4 ± 1.0	> 0.85
Azuma *et al.* [8]	$--$	$--$	$--$	2.38^{c}
Adelberger *et al.* [1]	$--$	$--$	$--$	3.25^{c}
Michelagnoli[a,d] [33]	< 1.0	$--$	$--$	> 0.66
Galinski *et al.*[b] [21]	< 1.8	< 2.5	$--$	> 0.44

TABLE 1.2

A SUMMARY OF PREVIOUS LIFETIME/WIDTH MEASUREMENTS FOR IMPORTANT STATES IN ^{15}O. A) MEASUREMENTS REPORTED WITH 90% CONFIDENCE LIMIT. B) MEASUREMENTS REPORTED WITH 68.3% CONFIDENCE LIMIT. C) REPORTED VALUE CALCULATED FROM R-MATRIX ANALYSIS. D) REPORTED IN PH.D. THESIS, NOT PEER REVIEWED.

1.5.2 Lifetime

As discussed, the Γ width of the 6.79 MeV subthreshold state is the dominant uncertainty on the total S-factor at zero energy, as illustrated by Fig. **??**. The literature to date on the lifetimes/widths of the important levels in ^{15}O are summarized in Table **??**. Some of the values present in the table are those extracted as a fit parameter from R-matrix analyses, instead of experimental measurements [1, 4, 8, 30, 36, 39**?**]. By having a dominant term of the calculation be a floating fit parameter, accuracy and reliability in the extrapolations are lost. Therefore, determination of this quantity experimentally is critical.

There are five measurements of the lifetime or width of the 6.79 MeV state "directly" [13, 21, 33, 40, 46], highlighted in red in Table **??**, and they are unfortunately disparate in their extracted values and have relatively large errors.

The first measurement was performed in 2001 by Bertone *et al.*, using the Doppler Shift Attenuation Method (DSAM) to determine the lifetime of the state. This technique will be discussed in further detail later. The authors populated the state through resonant capture of protons in the $E_p = 278$ keV state and observed the decaying γ-rays at three different angles. The measured lifetime for the 6.79 MeV state was determined to be $\tau = 1.60^{+0.75}_{-0.72}$ fs, corresponding to a width of $\Gamma = 0.41^{+0.34}_{-0.13}$ eV (determined by Equation 1.18).

At RIKEN, in 2004, Yamada *et al.* performed a measurement of the radiative width via Coulomb Excitation experiment [46] as an independent verification of the Bertone result. For this, ^{15}O nuclei were produced by fragmentation of an ^{16}O beam incident on a ^{9}Be target and then inelastically scattered off of a thick lead target. The de-excitation γ-rays were detected with an array of NaI (Tl doped) scintillation detectors. In order to disentangle the 6.79 MeV peak of interest from the 6.86 Mev peak in their spectrum, the authors compared the experimentally obtained spectrum from with the results of a Monte Carlo simulation. Due to the poor energy resolution of the detector system, the authors ultimately had difficulty separating the peaks and only reported an upper bound on the width, $\Gamma = 0.95^{+0.60}_{-0.95}$ eV, and a corresponding lifetime of $\tau = 0.69^{+1.10}_{-0.69}$ fs.

Four years later, Schürmann *et al.* published a new measurement of the lifetime using the DSAM technique and an improved experimental setup [40]. This measurement used a single high-purity germanium (HPGe) detector on a rotating track and measuring at many more angles ranging from $40 - 116^{\text{deg}}$, allowing for a check of asymmetries around the 90^{deg} point and reducing systematic uncertainties from the use of different detectors. Similar to the Bertone measurement [13], the authors populated the state of interest via the resonance at $E_p = 278$ keV. In contrast to the Bertone result and similar to the Yamada work, the authors in this case could not recommend a finite value for the measured lifetime, obtaining a lifetime upper limit of $\tau < 0.77$ fs.

In an attempt to provide another experimental technique for determining the lifetime, Galinski *et al.* performed another DSAM measurement at the TRIUMF facility [21]. The major difference this time, however, was that the reaction occurred in inverse kinematics (i.e. one where the heavier reaction input is accelerated towards the stationary, lighter one), emulating a result from over 50 years ago [22]. The ^{15}O in this experiment were produced via the $^{3}\text{He}(^{16}\text{O}, \alpha)^{15}\text{O}$ reaction with a ^{3}He-implanted gold-foil and the de-excitation γ-rays were detected with a clover HPGe detector (a single detector containing four separate Ge crystals) and filtered in coincidence with the reaction product α's. The authors then determined the lifetime with a Bayesian line-shape analysis of the spectra and found a most probable lifetime of $\tau = 0$ fs and an upper limit given by experimental

uncertainties of $\tau < 1.8$ fs with a 68.3% confidence limit. The authors, however, acknowledge that their result was statistics limited.

The final measurement of this lifetime comes from an unpublished doctoral dissertation by Michelagnoli in 2013 [33]. Similar to Galinski *et al.*, this measurement was done in inverse kinematics, with the $d(^{14}\mathrm{N}, ^{15}\mathrm{O})n$ reaction. The γ rays from this measurement were detected with the state-of-the-art AGATA Demonstrator array using γ-ray tracking for precision angular data and a lineshape analysis of the data was performed by comparing with the results of a Monte Carlo simulation in the Geant4 software. This work also obtained only an upper-bound on the lifetime, $\tau < 1.0$ fs with a 68.3% confidence limit. While this result is consistent with other literature values, it should nonetheless be taken with a grain of salt as it has not been peer-reviewed.

In aggregate, these results are unsatisfactory, with an error that is still uncomfortably large. Particularly, the DSAM results (with the exception of Galinski [21]) neglected the systematic uncertainties from the stopping power of the targets in their ultimate lifetime calculation. The forward kinematics reactions [13, 40] both used nitrogen-implanted tantalum-foils for the experiment (saturated to a composition of Ta_2N_3), but calculated the lifetimes assuming target densities and stopping powers equal to those of pure tantalum. However, in this lifetime range, the deceleration of the ^{15}O nuclei occurs in the region where the nitrogen is present in the lattice. Specifically, this means that the presence of the nitrogen has a significant effect on the actual stopping power. According to the authors of the respective works, by using accurate densities and stopping powers the inferred lifetimes obtained in their works would have changed by 100% [13] and 2% [40], respectively. In both, the authors also contend that their calculations are appropriate because they used an identical method to calculate the lifetime of the 5.18 MeV state, agreeing with literature values.

1.6 Thesis outline

In this dissertation, the results of a series of experiments and subsequent analyses performed to better understand the low energy behavior of the $^{14}\mathrm{N}(p,\gamma)^{15}\mathrm{O}$ will be presented. These include the measurement of the $^{14}\mathrm{N}(p,\gamma)^{15}\mathrm{O}$ reaction at the University of Notre Dame Nuclear Science Laboratory (NSL) and the Compact Accelerator System for Performing Astrophysical Research (CASPAR), located in the Sanford Underground Research Facility in the renovated Homestake Gold Mine in South Dakota, as well as a measurement of the lifetime of the 6.79 MeV level in ^{15}O also at the NSL.

An outline of the experimental techniques used in these measurements will be presented in Chap-

ter 2. There will be a brief overview of the equipment common to each of the measurements, with emphasis on the Van de Graaff accelerators and High-purity Germanium detectors used. Following this, the specific features of the different types of measurements and the facilities in which they were made will be presented.

Chapters 3 - 5 will present details on the different facets of the data reduction and analysis. The first of these, Chapter 3, presents the data for $^{14}\mathrm{N}(p,\gamma)^{15}\mathrm{O}$ taken at the NSL and CASPAR while detailing the process by which the cross-section and astrophysical S-factor were extracted. Shifting focus, Chapter 4 will focus on the Monte Carlo code that was developed and used to simulate the lifetime of the states in $^{15}\mathrm{O}$, presenting the results of these tests and displaying their ability to reproduce experimental cases. Finally, Chapter 5 will present the actual Doppler shift analysis of the data done to extract the lifetime of the 6.79 MeV state in $^{15}\mathrm{O}$. The validity of the method will be checked against other known levels populated in the reaction, like the states at 5.18 MeV and 6.17 MeV, respectively.

The cross-section information and newly measured lifetime will be utilized in a new R-matrix analysis of the $^{14}\mathrm{N}(p,\gamma)^{15}\mathrm{O}$ reaction, presented in Chapter 6. The new constraints these data provide on the low-energy behavior of the extrapolated S-factor will be provided, alongside a description of their impact to relevant astrophysical quantities.

Finally, the contents of this dissertation will be summarized in Chapter 7. This will present an overview of the described measurements, analysis, respective impacts, and future outlook.

CHAPTER 2

EXPERIMENTAL SETUP AND PROCEDURES

2.1 Introduction

This chapter is included to highlight some techniques and equipment commonly used in low-energy nuclear physics, with an emphasis on those used in this work. The discussion will be presented from the lens of the general to the specific, introducing general concepts for beam production and transport, acceleration systems, and radiation detection. Following the discussion of the scientific principles, I will detail the specifics of the equipment employed in this collective work. To that end, I will also highlight differences between the facilities and techniques employed when compared to common equipment for nuclear physics experiments

2.2 Experimental Equipment

2.2.1 Accelerators

First and foremost, low-energy nuclear physics (generally understood to be the regime in which incident kinetic energies for reactions are below 1 GeV, often even as low as sub-MeV) requires particle acceleration systems in order to bring beams and targets together. The most common techniques for accelerating ions are 1) to use strong electrostatic fields for a straight-line acceleration, such as in the Van de Graaff accelerator, or 2) by using a combination of electric and magnetic fields to accelerate the particles in cyclotron motion, aptly named a cyclotron. Van de Graaff accelerators are the most prominent of all accelerators, though, and are the type used in this work.

The basic idea of a Van de Graaff accelerator is shown in Fig. **??**. The governing principle is that a beam of ions produced in an ion source (Section 2.2.2) are manipulated by additional electromagnetic elements (Section 2.2.3) into an area of high electric potential. This high voltage is produced and maintained by continuously transporting positive charge from ground to a Faraday cage with a field free interior (referred to as the terminal, with voltage V_T). The positively charged ions, being in close proximity to the positively charged terminal feel a repulsive force, accelerating

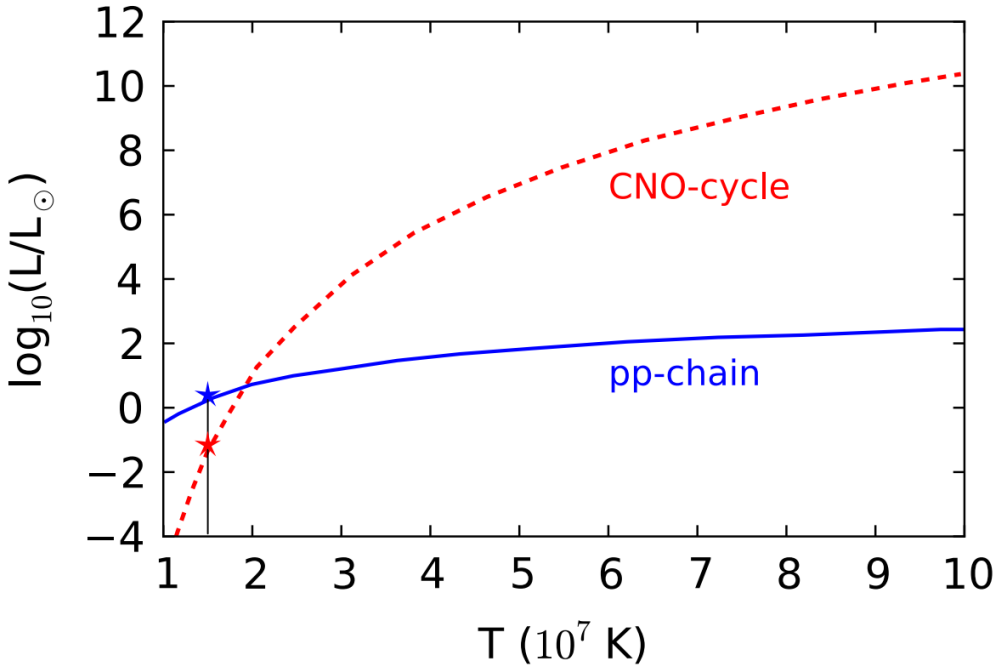

Figure 2.1. A diagram of a Van de Graaff accelerator [35]. The charge transportation in this figure is shown with a belt, like the JN accelerator model at CASPAR, while the 5U accelerator at the NSL uses a Pelletron chain.

the ions out of the terminal and through the machine. Upon exiting the accelerator, the ions have energy

$$E_{ion} = qV_T = \frac{1}{2} m_{ion} v_{ion}^2 \tag{2.1}$$

where V_T again is the terminal voltage and q is the charge state of the ion going through the accelerator, m_{ion} is the mass of the ion, and v_{ion} is the ion's velocity. When the terminal voltage is in MV, the beam energy is then provided in MeV. Specifically for the 5U accelerator, though, Equation 2.1 must be modified with an additional term. Inside the ion source, there is an electrostatic extractor, which transports the beam of ions out of the terminal and into the acceleration tube. With this correction, the beam energy for the 5U is given as

$$E_{ion} = q(V_{extractor} + V_T). \tag{2.2}$$

The charge is delivered to the terminal via a mechanical delivery system. The 5U Sta. Ana accelerator at the NSL uses four Pelletron chains citeHerb1974, each with its own power supply, while the JN Van de Graaff accelerator at CASPAR utilizes a rotating belt. In either case, the entire charging system is contained inside of a pressurized tank of insulating gas, SF_6 for the 5U and CO_2 for the JN, reducing the chance of a terminal discharge to ground from dielectric breakdown. This is not the only element to ensure the operational stability of the machine. The charging systems supply charge continuously to the terminal. However, charge is always being removed from the terminal via three primary pathways: 1) the beam of ions passing through the accelerator, 2) the resistive column, and 3) the corona system. In order to maintain stability, the currents that pass through these systems must always be in balance according to Kirchoff's Rule,

$$I_{chains} = I_{beam} + I_{column} + I_{corona}. \tag{2.3}$$

The column is actually a series of equipotential hoops connected by equal resistors. Each conducting hoop provides a small step down in voltage from the terminal, ensuring that the beam of ions feel a smooth potential gradient throughout their acceleration. These can be seen in Fig. **??**, showing an interior view of Sta. Ana accelerator tank.

The corona system is the real workhorse maintaining the stability of the accelerator's charging systems. As small irregularities can be present between different links in the Pelletron chains or the belt itself, the corona system is responsible for precise second-by-second compensation. The mechanical part of the system consists of an arm with sharp metal points on the end which can be moved towards and away from the terminal to draw away current. On the back end, however, it also is controlled by a voltage feedback system to adjust the current draw, keeping the terminal at a constant voltage. The feedback for the system is provided either by an external reference through a generating voltmeter or from the beam itself as it passes through an analyzing dipole magnet at the exit of the accelerator. As the beam passes through the magnet it will pass through a set of slits. If V_T changes slightly, the energy of the beam will subsequently change, impacting the balance of the beam on the exit slits. This change in current will be fed back to the corona system, which in turn will compensate by changing the charge delivered to the terminal in order to maintain the slit balance. With this, V_T can be kept incredibly steady, within roughly 1 kV for every MV on the terminal. This is the biggest advantage of a Van de Graaff accelerator over a cyclotron. Intrinsically, this acceleration system makes nuclear experiments possible through monoenergetic beams.

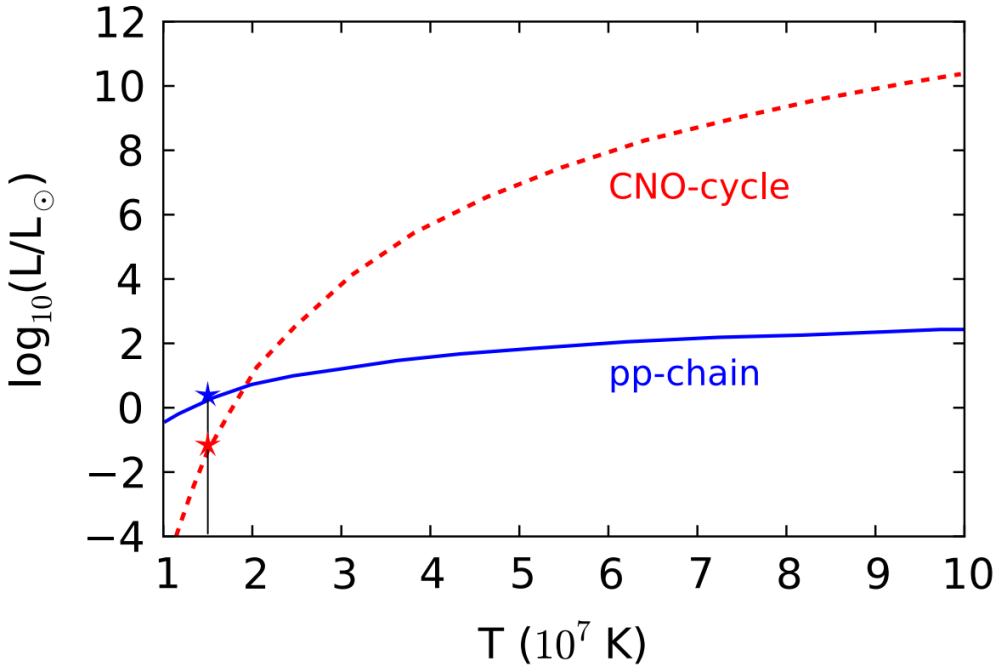

Figure 2.2. View inside the Sta. Ana accelerator tank, showing the equipotential hoops as part of the column.

2.2.2 Ion sources

A key item for the successful operation of any accelerator is the ion source, which produces the beams of charged particles used in experiments. Generating such beams is not a trivial task and, as such, many methods have been developed for achieving this. The two types relevant to this work, however, are the Electron-Cyclotron Resonance (ECR) ion source, used in the Sta. Ana accelerator at the NSL, and the radio frequency (RF) ion source, utilized in the JN accelerator at CASPAR. Both systems are housed within their respective accelerator terminals, which acts as a Faraday cage and shields the internal components from external fields. Additionally, both systems operate on the same basic principle, namely that a given gas is ionized through the use of electron collisions in the source, but the mode of electron excitation is different.

For the specifics of the ECR system, the 5U employs a Pantechnik Nanogen 14.5 GHz ECR source. This utilizes the cyclotron resonance of electrons (as the name obviously implies) to produce and maintain a plasma.

During operation, neutral gas (which includes the element to be accelerated as a component) is injected into a cavity surrounded by magnets. These magnets provide a superposition of axial and multipole fields in order to achieve a minimum at the center of the cavity increasing radially outwards with the goal of confining and stabilizing the generated ions. A cartoon depiction of such a system is presented in Fig. **??**. In order to generate the ions from neutral gas, a current is supplied to the chamber by a negative bias probe providing a constant supply of charge. From this, then, electrons are stripped and continually accelerated in cyclotron motion following the familiar cyclotron frequency relation:

$$\omega_{ecr} = \frac{e|B|_{ECR}}{m_e} = \omega_{rf} \tag{2.4}$$

where ω_{ecr} is the frequency for the cyclotron resonance of electrons in a given magnetic field B_{ECR}, e and m_e are the charge and mass of the electron, respectively, and ω_{rf} is the frequency supplied by a radio radio-frequency (RF) power supply. This last term is included to highlight that during operation this is supplied externally and controlled in the use of the source in order to produce the plasma. After ionization, the magnetic configuration confines the plasma radially, while the axial magnetic field (provided by the extractor) pushes it through the cavity towards the exit of the source. Upon exiting the chamber and the Faraday cage of the terminal, the positive ions are next to a the positively charged terminal at high voltage, thus accelerating the ions.

An ECR ion source has many advantages of over other common ion source designs. The primary

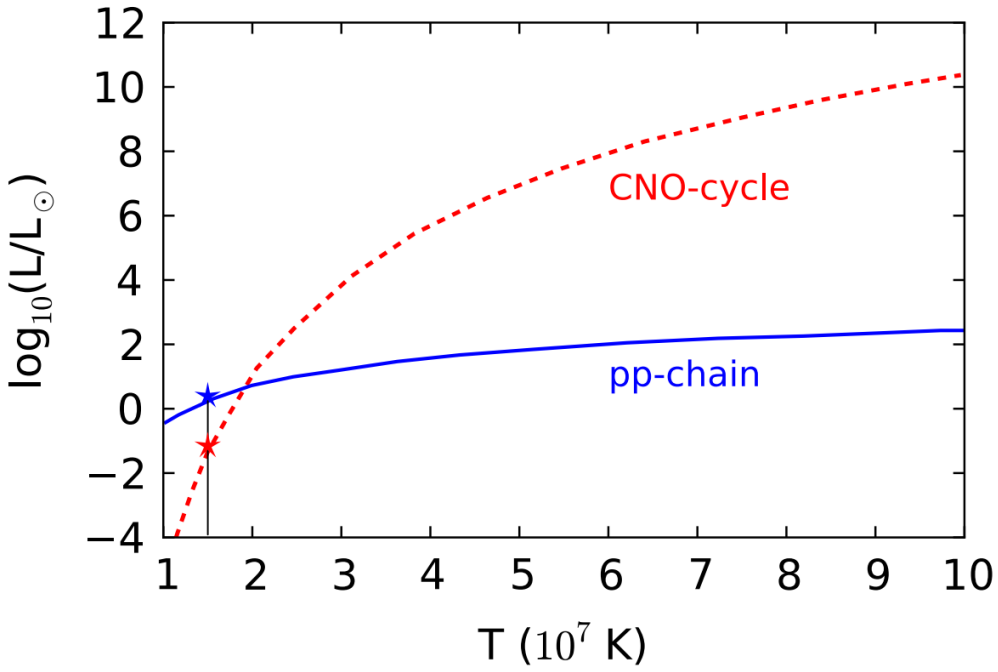

Figure 2.3. Depiction of the interior of an ECR ion source with magnetic components labeled citeMelin1997. This example shows a source operating from left to right, with the gas and RF generator inputs depicted as well as the exit for the ions. As discussed in the text, the combination of magnets confines the plasma in the center as it is pushed from left to right and out of the source.

advantage lies in its ability to deliver high-intensity beams (as much as hundreds of μA). For use in nuclear astrophysics experiments, such as the ones performed in this work, low cross sections are a problem to overcome, which is mitigated through this higher production. Additionally, due to the relatively simple restrictions on the inputs, these sources can provide a wide array of species, as they can produce beams of nearly anything that can be made into a gas, and exhibit long term stability, reliability, and longevity citeMelin1997. On the other hand, however, ECR ion sources also have some disadvantages compared to other common sources. One main drawback is that the ions are produced through the production of a plasma, meaning they are not directly controlled by any operational parameter citeMelin1997. This leads to complicated tuning and sensitive operation, experimentally. Additionally, such sources are only capable of generating positive beams and can therefore only be utilized in single stage accelerators. Finally, due to the size of these ion sources and their necessary components, they are often impractical. In order to employ one in the Sta. Ana accelerator, the accelerator design had to be vertical. If the accelerator had been horizontal (like the other accelerators at the NSL) the torque generated by the ECR ion source would have shattered the acceleration column. Vertically, however, the source is stable inside the accelerator. Unfortunately, the choice to build and use the accelerator vertically is not one that every lab can make.

The radio frequency (RF) ion source utilized at CASPAR operates on a very similar principle to the ECR ion source inside the Sta. Ana accelerator. A depiction of the RF ion source's components is given in Fig. **??**. In this case, the source chamber is a glass tube filled with a monoatomic gas, at CASPAR the only options are ^{1}H and ^{4}He. Electromagnetic coils are placed on both sides of this tube and generate RF waves in the tube, between the rings. In response to these waves, the electrons oscillate through and collide with the source gas, ionizing it. At the rear of the glass tube, an electrode supplies a constant, positive voltage (with respect to the terminal), forcing any ionized atoms towards the exit of the source. Upon leaving the source, as with the ECR ion source, the ions are accelerated because of their repulsion to the positively charged terminal.

The RF ion source at CASPAR was also recently refurbished before installation, leaving it capable of beam production at even higher intensities than the ECR ion source inside the Sta. Ana accelerator. It can produce beams up to 150 μA, enabling similar high-intensity experiments. Another similarity to the ECR ion source is that it provides excellent operational stability and reliability. It does, however have significant drawbacks as well. The first and foremost of these is the degredation of the ion source canal. Operating the source causes a buildup on the exit canal

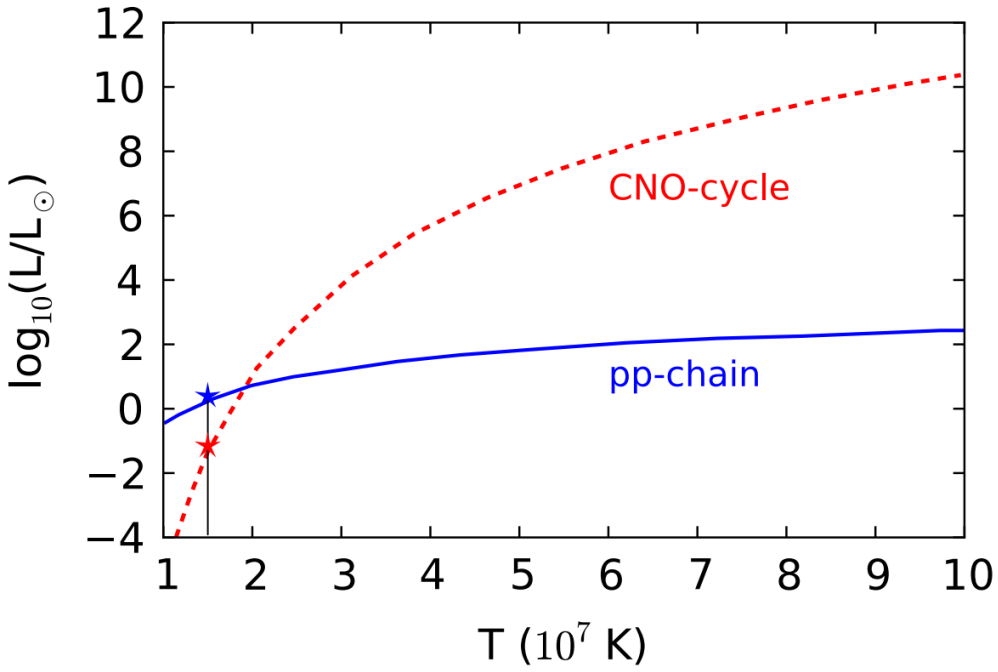

Figure 2.4. Depiction of the interior of a RF ion source with magnetic components labeled citeLi2015. The coils on either side provide the field to ionize the gas, whereas the probe on top provides the field necessary to extract the ions from the chamber.

of the source tube (higher intensity operation accelerates this process), necessitating significant maintenance. Additionally, the glass tube housing the plasma is quite sensitive. If power is supplied to the source when gas is not present, significant damage to the tube can occur. This is only mitigated with vigilant operation. The other major drawback is that the source is only capable of providing beams of two species (typically hydrogen and helium). In order to change the delivered species, a full tank opening and source alignment is required.

Altogether, though, these sources are ideal for this work. They provide the necessary ion beams at high intensity, enabling the experiments.

2.2.3 Beam transport

Upon exiting the accelerator, the beam envelope contains a distribution of different masses, charges, and energies because the ion sources are indiscriminate in their production methods. For example, an ion source might produce some ionized diatomic gas, instead of monoatomic, like producing $^1\mathrm{H} + {}^1\mathrm{H}$ due to insufficient breakup of the source gas. However, all particles created in the same ionization state will have the same energy, dictated by Equation 2.2. In order to filter such contaminants out of the beam, analyzing magnets are employed. These are typically 90^{deg} dipole magnets, also utilizing the cyclotron motion of ions in a magnetic field in order to select a given type of particle at a specific energy. These magnets are typically located at the exit of accelerators, and, due to their fixed size, have a fixed radius, R_{am}, through which a beam can pass. Therefore, for a given particle of mass m, energy E, and charge state q, the magnetic field, B_{am}, inside the analyzing magnet can be tuned to allow through only a specific particle/energy combination by

$$B_{am} = \frac{\sqrt{2mE}}{qR_{am}} = \frac{\sqrt{2m}}{qR_{am}}\sqrt{E} = k\sqrt{E} \tag{2.5}$$

, where k is a constant for a unique combination of particle and charge state. This separates the in-beam contaminants from the ions of experimental interest.

In order to deliver the beam of ions to the target chamber and experimental hall, a series of steering and focusing elements are placed along the beam pipes. As the beam is self-repulsive due to it all being the same charge, these are necessary to contain the beam and keep its intensity at acceptable levels for experimental purposes. They also allow adjustment of the beam's position in order to deliver it to a specific experimental setup and allowing for simple transitions between different target locations.

Vacuum systems are important components of the beam production and experimental operation.

All experimental components, like the ion source chamber, acceleration tubes, target chamber, and connecting beam pipes need to be free of residual gas. If not, the beam quality would suffer dramatically, collisions of the beam with the remaining atmosphere would cause significant intensity and energy losses, preventing transport and, ultimately, the measurement. In order to maintain an experimental vacuum level (typically $\sim 10^{-7}$ Torr), a series of metal pipes run from the ion source to the target chamber. These are connected by air-tight gaskets and have isolating valves employed with high-vacuum pumps (cryogenic or turbomolecular) along the line. These enable easier maintenance or changing of experimental conditions without destroying the vacuum created through the entire beam line. Without high-vacuum, there would be additional adverse effects on the target quality. Contaminants, typically hydrocarbons, present in residual gas can accumulate on the surface of the target due to the beam heating the surface. This is unwanted, as it not only provides an additional layer of energy loss for the beam before interacting with the target but also a significant contaminant in experimental results due to carbon's high cross-section.

Besides maintaining clean, high-vacuum near a target, another common method for reducing the carbon build-up on experimental surfaces is to utilize a so called cold trap in front of a target. A cold trap is is a liquid nitrogen cooled copper pipe designed to be nearly the same size and shape as the beam pipe to prevent it from interfering with an experiment. An example of a cold trap like the one used in this work is shown in Fig. **??**. The cold trap works much like a cryogenic pump. By cooling the copper pipe with liquid nitrogen, the residual hydrocarbons in the beam pipe and target chamber will condense on the surface of the pipe, trapping them before most can reach the target and cause carbon buildup.

2.2.4 Radiation detection

types

photon interactions with matter

HPGe

2.3 The CASPAR facility and cross-section measurements

This set of data was taken over the course of five* separate experiments. The first occurred at the University of Notre Dame's Nuclear Science Laboratory (NSL) in January of 2018 and covered the proton energy range of $E_p = 800$ - 1200 keV. The experiment was then continued at the Compact Accelerator System for Performing Nuclear Astrophysics (CASPAR) facility at the Sanford Under-

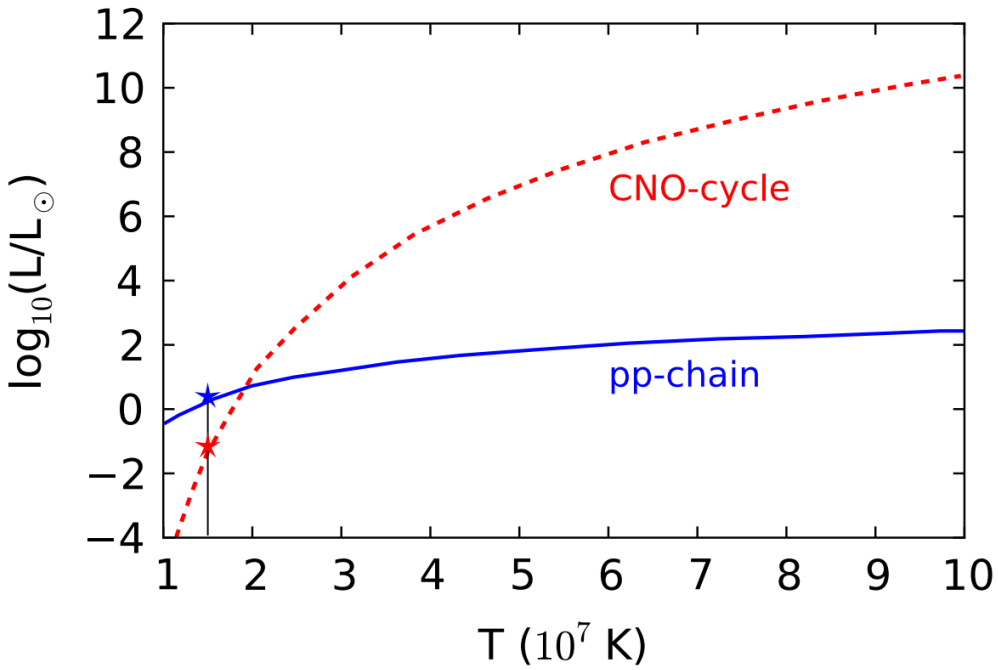

Figure 2.5. Depiction of a cold trap used in this work. The reservoir on top is filled with liquid nitrogen and connected to the copper pipe inside the target chamber, causing the copper pipe inside to be cooled. At cold temperatures, most of the contaminants present in the beam pipe will condense on the copper pipe instead of building up on the target surface.

ground Research Facility located in Lead, South Dakota in three increments: February 2018, May 2018, and August / September 2018. These measurements covered the energy range from E_p = 270 - 1200 keV, in order to measure the $^{14}N(p,\gamma)^{15}O$ reaction cross-section to compare the performance of the CASPAR facility to an above-ground laboratory. Finally, in MONTH TIME DATE THING, the final experiment was completed at the NSL, focusing on obtaining the lifetime of the 6793 keV state in ^{15}O.

Reiterate why we went underground and its advantages Background comparison

Calibration of the analyzing magnet?

Describe experiment (PJ)

2.4 Lifetime measurement

2.4.1 The Doppler-Shift Attsenuation Method for lifetime measurements

Nuclear lifetimes are important observables to measure because they provide a link to understanding the strong nuclear force. They are necessary to determine the reduced transition probabilities which are one of the most important probes of nuclear structure and the forces governing the behavior of nuclei.The Doppler Shift Attenuation Method (DSAM) is a well characterized method for determining the lifetimes of excited nuclear states that decay via gamma emission in the range of 10^{-11} - 10^{-15} s [16]. The ranges where DSAM is applicable are compared with other common methods for determining nuclear lifetimes in Fig. **??**.

The basic idea of DSAM is to produce an excited nucleus inside of a dense target in which the reaction product will decay. The de-excitation of the nucleus then takes place either while the nucleus is slowing down or after it stops, depending on the lifetime of the specific state and the stopping within the target. Then, as is true with the classical Doppler shift, the energy of the emitted γ-rays are shifted depending on their emission angle relative to the motion of their source, the decaying nucleus. Thus, γ's emitted at different velocities during the slow-down and detected at given angles will have a spread of energies. Specifically, for a given nucleus decaying at a time t with a speed of $v(t)$, the Doppler shifted energy of the gamma ray, E_γ, is

$$E_\gamma = E_0 \left(1 + \frac{v(t)}{c}\cos(\theta)\right), \tag{2.6}$$

where E_0 is the energy of the decay for a nucleus at rest, c is the speed of light, and θ is the lab angle between the momentum vectors of the decaying nucleus and gamma ray, respectively. A depiction

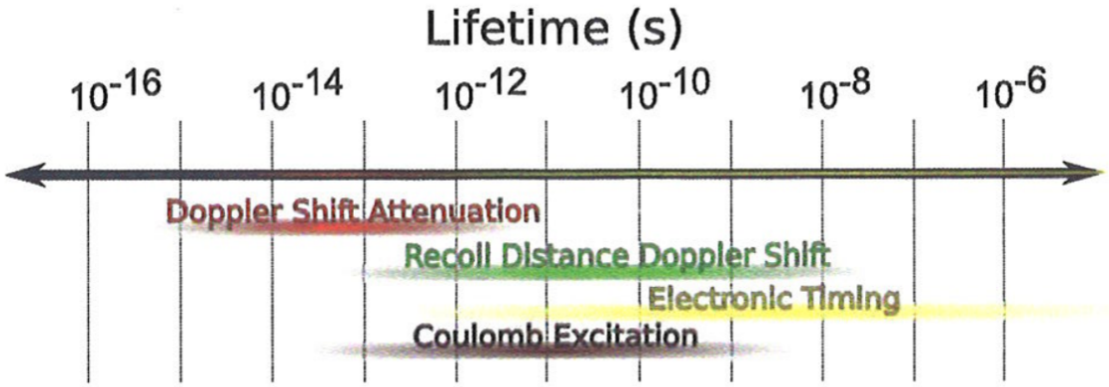

Figure 2.6. Ranges over which the different lifetime measuring techniques are valid (Obtained via personal communication with M.K. Smith in 2017). **CHANGE THIS REFERENCE**

of this scenario is given in Fig. **??**.

As the nuclear decay process is statistical in nature, the measured spectrum of gamma energies for a particular transition is a continuous distribution of energies from the unshifted, rest energy peak to the maximally Doppler shifted peak. As Equation 2.6 was specific to a single transition, it is necessary to consider the entire sample of decays measured. By defining the average velocity of all nuclei at the time of decay, $\overline{v}$, the initial velocity of all recoiling nuclei, v_0, and their ratio, $F(\tau)$, called the attenuation factor, it is possible to relate the behavior of the entire distribution to the lifetime of the state. This is

$$E_\gamma = E_0 \left(1 + F(\tau)\beta_0 \cos(\theta)\right), \tag{2.7}$$

where $\beta_0 = v_0/c$ is the relativistic velocity factor. $F(\tau)$ therefore provides an analytical relation between the nuclear lifetime and the measured Doppler shift, given by Blaugrund in 1966 [16] as

$$F(\tau)\beta_0 = \frac{1}{\tau}\int_0^\infty \beta(t) \exp\left(\frac{t}{\tau}\right) dt, \tag{2.8}$$

where $\beta(t) = v(t)/c$ is the time dependent relativistic velocity factor. The devil, however, is in the details of calculating $\beta(t)$, since it is reliant on stopping powers of the nuclei in the target material, implying an accurate knowledge of the target composition and population pattern of the nucleus. In some cases the feeding is not well known and for nearly all cases, there is an estimated uncertainty

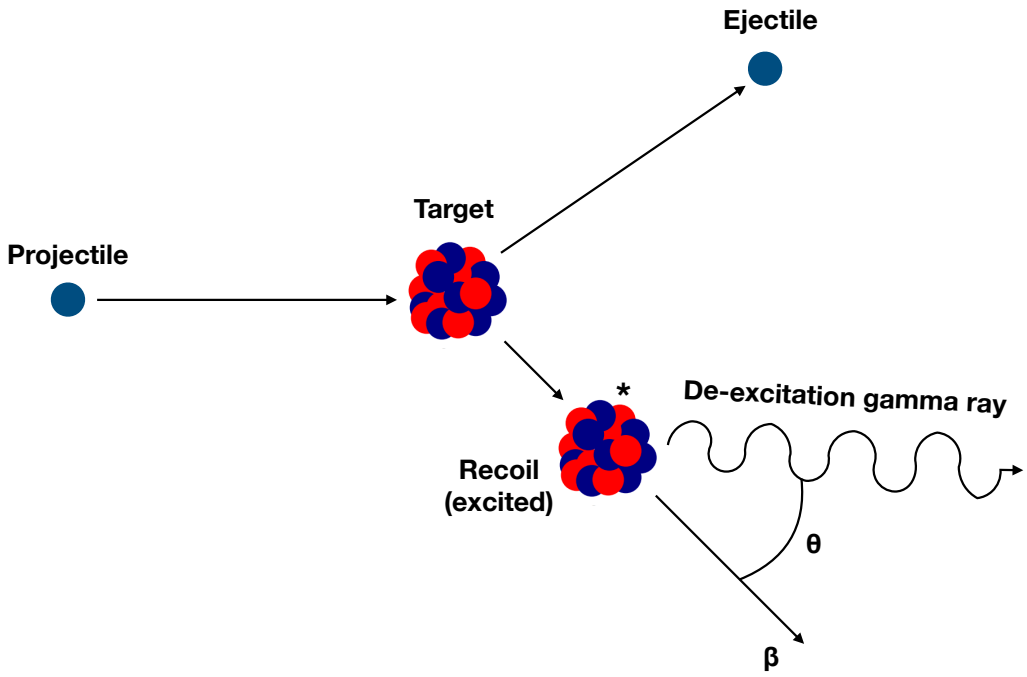

Figure 2.7. A generic nuclear reaction showing the creation of an excited nucleus and subsequent decay, causing a Doppler shift in the measured energy of the γ ray.

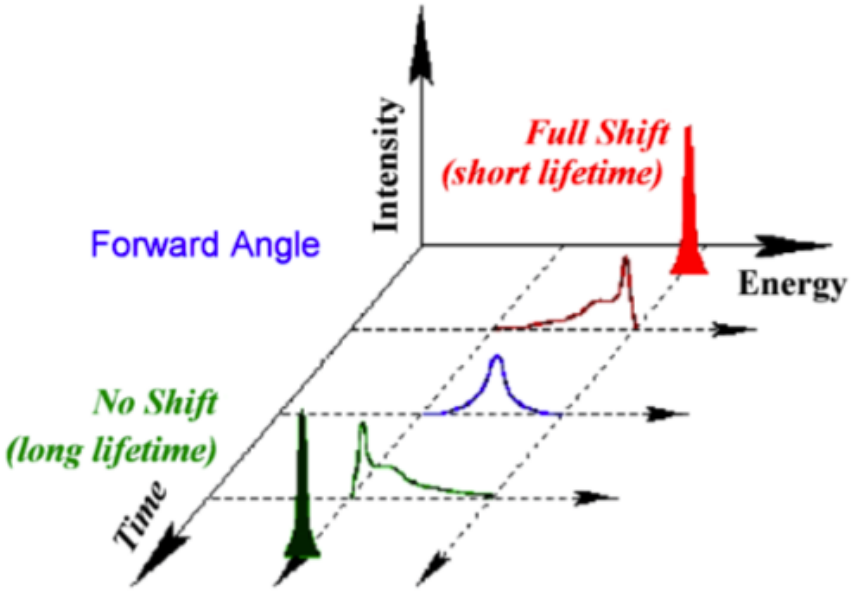

Figure 2.8. The effect of the nuclear lifetime on the measured gamma spectrum for a given experimental scenario [38]. In forward angles, the γ's energy is shifted to higher values, while the the measured energy of the γ is lower at backward angles, with the maximum shift in either direction coming when the γ is emitted in a direction parallel to the motion of the decaying nucleus. A γ emitted at 90^{deg} is unshifted and unbroadened.

in the assessment of stopping powers of materials to be at least 10%.

It is important to note that the Doppler shift can either increase or decrease the energy of the measured γ ray, depending on whether the emitted gamma ray is at forward or backward angles relative to the nucleus' motion. Fig. **??** shows the Doppler effect on a measured γ spectrum, shifting the energy according to the measured angle. It is evident that the lifetime of a particular excited state has a dramatic effect on the location and shape of this distribution, for the longer a specific lifetime is, the broader its measured distribution will be (and vice versa) while the shift in the centroid of the peak will be lower than that of short lifetimes where the nucleus has a relatively higher velocity upon decay.

Therefore, by performing a lineshape analysis on the distribution of the measured γ's and a mapping of the distribution's shift with angle one can determine the nuclear lifetime. The procedure for the Doppler shift determination is particularly straightforward. By plotting the resulting centroids measured for the gamma distribution vs the $\cos(\theta)$, one should obtain a straight line, the slope of

which is the product $E_0\beta_0 F(\tau)$. So, for a given experimental approach with the same reaction and targets, this slope and therefore attenuation factor should match. This was not the case for the Bertone *et al.* and Schürmann *et al.* works [13, 40], where the authors used the same reaction on ostensibly the same targets and reached incongruous $F(\tau)$ values.

2.4.2 Target production

Why Implantation Seuthe How did we produce them and why

2.4.3 Measurement at Notre Dame

How did we do it Highlight similarities and differences to previous measurements.

CHAPTER 3

CROSS SECTION DATA REDUCTION AND ANALYSIS

3.1 Introduction

$^{14}\mathrm{N}(p,\gamma)^{15}\mathrm{O}$

3.2 Energy calibration

3.3 Efficiency

3.4 Summing corrections

3.5 Target characterization

3.6 Cross-section determination

CHAPTER 4

MONTE CARLO SIMULATIONS FOR LIFETIME MEASUREMENTS WITH DSAM

4.1 Monte Carlo methods

4.2 Simulations with the Geant4 package

4.3 Determining a nuclear lifetime

CHAPTER 5

MEASURED LIFETIMES

5.1 Lifetime of the 5.18 MeV state in ^{15}O

5.2 Lifetime of the 6.17 MeV state in ^{15}O

5.3 Lifetime of the 6.79 MeV state in ^{15}O

CHAPTER 6

R-MATRIX ANALYSIS

6.1 Fits to the capture data

6.2 Inclusion of the new lifetime

CHAPTER 7

RESULTS AND CONCLUSIONS

BIBLIOGRAPHY

1. E. Adelberger and a. García. Solar fusion cross sections. II. The pp chain and CNO cycles. *Rev. Mod. ...*, 83(March), 2011. URL http://rmp.aps.org/abstract/RMP/v83/i1/p195{_}1.

2. E. Adelberger, S. Austin, J. Bahcall, A. Balantekin, G. Bogaert, L. Brown, L. Buchmann, F. Cecil, A. Champagne, L. de Braeckeleer, C. Duba, S. Elliott, S. J. Freedman, M. Gai, G. Goldring, C. Gould, A. Gruzinov, W. Haxton, K. M. Heeger, E. Henley, C. Johnson, M. Kamionkowski, R. Kavanagh, S. Koonin, K. Kubodera, K. Langanke, T. Motobayashi, V. Pandharipande, P. Parker, R. Robertson, C. Rolfs, R. Sawyer, N. J. Shaviv, T. Shoppa, K. Snover, E. Swanson, R. E. Tribble, S. Turck-Chieze, and J. Wilkerson. Solar Fusion Cross Sections. *Rev. Mod. Phys.*, 70(4):48, 1998. ISSN 0034-6861. doi: 10.1103/RevModPhys.70.1265. URL http://arxiv.org/abs/astro-ph/9805121.

3. R. A. Alpher, H. Bethe, and G. Gamow. The Origin of Chemical Elements. *Phys. Rev.*, 73(7), 1948.

4. C. Angulo and P. Descouvemont. The 14 N(p,g)15O low-energy S-factor. *Nucl. Phys. A*, 690: 755–768, 2001.

5. C. Angulo, M. Arnould, M. Rayet, P. Descouvemont, D. Baye, C. Leclercq-Willain, A. Coc, S. Barhoumi, P. Aguer, C. Rolfs, R. Kunz, J. Hammer, A. Mayer, T. Paradellis, S. Kossionides, C. Chronidou, K. Spyrou, S. Degl'Innocenti, G. Fiorentini, B. Ricci, S. Zavatarelli, C. Providencia, H. Wolters, J. Soares, C. Grama, J. Rahighi, A. Shotter, and M. Lamehi Rachti. A compilation of charged-particle induced thermonuclear reaction rates. *Nucl. Phys. A*, 656(1):3–183, 1999. ISSN 03759474. doi: 10.1016/S0375-9474(99)00030-5. URL http://linkinghub.elsevier.com/retrieve/pii/S0375947499000305.

6. C. Angulo, A. E. Champagne, and H. P. Trautvetter. R-matrix analysis of the 14N(p,g)15O astrophysical S-factor. *Nucl. Phys. A*, 758:391–394, 2005. doi: 10.1016/j.nuclphysa.2005.05.070.

7. M. Asplund, N. Grevesse, A. J. Sauval, and P. Scott. The Chemical Composition of the Sun. *Annu. Rev. Astron. Astrophys.*, 46, 2009. doi: 10.1146/annurev.astro.46.060407.145222.

8. R. E. Azuma, E. Uberseder, E. C. Simpson, C. R. Brune, H. Costantini, R. J. De Boer, J. Görres, M. Heil, P. J. Leblanc, C. Ugalde, and M. Wiescher. AZURE: An R-matrix code for nuclear astrophysics. *Phys. Rev. C - Nucl. Phys.*, 81(4):1–17, 2010. ISSN 05562813. doi: 10.1103/PhysRevC.81.045805.

9. J. N. Bahcall and A. M. Serenelli. NEW SOLAR OPACITIES, ABUNDANCES, HELIOSEISMOLOGY, AND NEUTRINO FLUXES John N. Bahcall and Aldo M. Serenelli. *Astrophys. J.*, 04:85–88, 2005.

10. J. N. Bahcall and A. M. Serenelli. HOW DO UNCERTAINTIES IN THE SURFACE CHEMICAL COMPOSITION OF THE SUN AFFECT THE PREDICTED SOLAR NEUTRINO FLUXES ? *Astrophys. J.*, pages 530–542, 2005.

11. D. Bemmerer. *Experimental study of the 14N(p,g)15O reaction at energies below the Coulomb barrier*. PhD thesis, Technischen Universitat Berlin, 2004.

12. D. Bemmerer, F. Confortola, A. Lemut, R. Bonetti, C. Broggini, P. Corvisiero, H. Costantini, J. Cruz, A. Formicola, Z. Fülöp, G. Gervino, A. Guglielmetti, C. Gustavino, G. Gyürky, G. Imbriani, A. Jesus, M. Junker, B. Limata, R. Menegazzo, P. Prati, V. Roca, C. Rolfs, D. Rogalla, M. Romano, C. Rossi-Alvarez, F. Schümann, E. Somorjai, O. Straniero, F. Strieder, F. Terrasi, and H. P. Trautvetter. Low energy measurement of the 14N(p, g)15O total cross section at the LUNA underground facility. *Nucl. Phys. A*, 779:297–317, 2006. ISSN 03759474. doi: 10.1016/j.nuclphysa.2006.09.001.

13. P. F. Bertone, A. E. Champagne, D. Powell, C. Iliadis, S. Hale, and V. Hansper. Lifetime of the 6793-keV State in 15O. *Phys. Rev. Lett.*, 87(15):152501, 2001. ISSN 0031-9007. doi: 10.1103/PhysRevLett.86.4189. URL `http://link.aps.org/doi/10.1103/PhysRevLett.86.4189`.

14. P. F. Bertone, A. E. Champagne, M. Boswell, C. Iliadis, S. Hale, V. Hansper, and D. Powell. 14N(3He,d)15O as a probe of direct capture in the 14N(p,g)15O reaction. *Phys. Rev. C*, 66(4): 055804, 2002. ISSN 0556-2813. doi: 10.1103/PhysRevC.66.048801. URL `http://link.aps.org/doi/10.1103/PhysRevC.66.048801`.

15. C. A. Bertulani and T. Kajino. Frontiers in nuclear astrophysics. *Prog. Part. Nucl. Phys.*, 89: 56–100, 2016. ISSN 01466410. doi: 10.1016/j.ppnp.2016.04.001. URL `http://dx.doi.org/10.1016/j.ppnp.2016.04.001`.

16. A. E. Blaugrund. Notes on Doppler-shift lifetime measurements. *Nucl. Phys.*, 88(3):501–512, 1966. ISSN 0029-5582. doi: 10.1016/0029-5582(66)90409-3. URL `http://www.sciencedirect.com/science/article/pii/0029558266904093`.

17. B. W. Carroll and D. A. Ostlie. *An Introduction to Modern Astrophysics*. 2nd edition, 2007.

18. S. Daigle, K. J. Kelly, A. E. Champagne, M. Q. Buckner, C. Iliadis, and C. Howard. Measurement of the Ec.m. = 259 keV resonance in the 14N(p,g)15O reaction. *Phys. Rev. C*, 94(025803), 2016. ISSN 2469-9985. doi: 10.1103/PhysRevC.95.015806. URL `http://link.aps.org/doi/10.1103/PhysRevC.95.015806`.

19. B. D. Fields. The Primordial Lithium Problem. *Annu. Rev. Nucl. Part. Sci.*, 61(1):47–68, nov 2011. ISSN 0163-8998. doi: 10.1146/annurev-nucl-102010-130445. URL `http://www.annualreviews.org/doi/abs/10.1146/annurev-nucl-102010-130445`.

20. A. Formicola, G. Imbriani, H. Costantini, C. Angulo, D. Bemmerer, R. Bonetti, C. Broggini, P. Corvisiero, J. Cruz, P. Descouvemont, Z. Fülöp, G. Gervino, A. Guglielmetti, C. Gustavino, G. Gyürky, A. P. Jesus, M. Junker, A. Lemut, R. Menegazzo, P. Prati, V. Roca, C. Rolfs, M. Romano, C. Rossi Alvarez, F. Schümann, E. Somorjai, O. Straniero, F. Strieder, F. Terrasi, H. P. Trautvetter, A. Vomiero, and S. Zavatarelli. Astrophysical S-factor of 14N(p,γ)15O. *Phys. Lett. Sect. B Nucl. Elem. Part. High-Energy Phys.*, 591(1-2):61–68, 2004. ISSN 03702693. doi: 10.1016/j.physletb.2004.03.092. URL `http://dx.doi.org/10.1016/j.physletb.2004.03.092`.

21. N. Galinski, S. K. Sjue, G. C. Ball, D. S. Cross, B. Davids, H. Al Falou, A. B. Garnsworthy, G. Hackman, U. Hager, D. A. Howell, M. Jones, R. Kanungo, R. Kshetri, K. G. Leach, J. R. Leslie, M. Moukaddam, J. N. Orce, E. T. Rand, C. Ruiz, G. Ruprecht, M. A. Schumaker, C. E. Svensson, S. Triambak, and C. D. Unsworth. Lifetime measurements of states in O 15. *Phys. Rev. C - Nucl. Phys.*, 90(3):1–11, 2014. ISSN 1089490X. doi: 10.1103/PhysRevC.90.035803.

22. R. D. Gill, J. S. Lopes, O. Hausser, and H. J. Rose. Lifetime Measurement in Mass-15 Nuclei. *Nucl. Phys. A*, 121:209–223, 1968.

23. C. Iliadis. *Nuclear Physics of Stars*. 2nd edition, 2007.

24. G. Imbriani, H. Costantini, A. Formicola, D. Bemmerer, R. Bonetti, C. Broggini, P. Corvisiero, J. Cruz, Z. Fülöp, G. Gervino, A. Guglielmetti, C. Gustavino, G. Gyürky, A. P. Jesus, M. Junker, A. Lemut, R. Menegazzo, P. Prati, V. Roca, C. Rolfs, M. Romano, C. Rossi Alvarez, F. Schümann, E. Somorjai, O. Straniero, F. Strieder, F. Terrasi, H. P. Trautvetter, A. Vomiero, and S. Zavatarelli. The bottleneck of CNO burning and the age of Globular Clusters. *Astron. Astrophys.*, 420(2):625–629, 2004. ISSN 0004-6361. doi: 10.1051/0004-6361:20040981. URL `http://www.aanda.org/10.1051/0004-6361:20040981`.

25. G. Imbriani, H. Costantini, A. Formicola, A. Vomiero, C. Angulo, D. Bemmerer, R. Bonetti, C. Broggini, F. Confortola, P. Corvisiero, J. Cruz, P. Descouvemont, Z. Fülöp, G. Gervino, A. Guglielmetti, C. Gustavino, G. Gyürky, A. P. Jesus, M. Junker, J. N. Klug, A. Lemut, R. Menegazzo, P. Prati, V. Roca, C. Rolfs, M. Romano, C. Rossi-Alvarez, F. Schümann, D. Schürmann, E. Somorjai, O. Straniero, F. Strieder, F. Terrasi, and H. P. Trautvetter. S-factor of 14N(p,g)15O at astrophysical energies. *Eur. Phys. J. A*, 25(3):455–466, 2005. ISSN 14346001. doi: 10.1140/epja/i2005-10138-7.

26. J. José and C. Iliadis. Nuclear astrophysics: The unfinished quest for the origin of the elements. *Reports Prog. Phys.*, 74(9), 2011. ISSN 00344885. doi: 10.1088/0034-4885/74/9/096901.

27. A. M. Lane and R. G. Thomas. R-matrix theory of nuclear reactions. *Rev. Mod. Phys.*, 30(2): 257–353, 1958. ISSN 00346861. doi: 10.1103/RevModPhys.30.257.

28. A. Lemut, D. Bemmerer, F. Confortola, R. Bonetti, C. Broggini, P. Corvisiero, H. Costantini, J. Cruz, A. Formicola, Z. Fülöp, G. Gervino, A. Guglielmetti, C. Gustavino, G. Gyürky, G. Imbriani, A. P. Jesus, M. Junker, B. Limata, R. Menegazzo, P. Prati, V. Roca, D. Rogalla, C. Rolfs, M. Romano, C. Rossi Alvarez, F. Schümann, E. Somorjai, O. Straniero, F. Strieder, F. Terrasi, and H. P. Trautvetter. First measurement of the 14N(p,6)15O cross section down to 70 keV. *Phys. Lett. Sect. B Nucl. Elem. Part. High-Energy Phys.*, 634(5-6):483–487, 2006. ISSN 03702693. doi: 10.1016/j.physletb.2006.02.021.

29. Q. Li, J. Görres, R. J. DeBoer, G. Imbriani, A. Best, A. Kontos, P. J. LeBlanc, E. Uberseder, and M. Wiescher. Cross Section Measurement of 14N(p,γ)15O in the CNO Cycle. *Phys. Rev. C*, 93(4):055806, 2016. ISSN 0556-2813. doi: 10.1103/PhysRevC.93.055806. URL `http://link.aps.org/doi/10.1103/PhysRevC.91.045804`.

30. M. Marta, A. Formicola, G. Gyürky, D. Bemmerer, C. Broggini, A. Caciolli, P. Corvisiero, H. Costantini, Z. Elekes, Z. Fülöp, G. Gervino, A. Guglielmetti, C. Gustavino, G. Imbriani, M. Junker, R. Kunz, A. Lemut, B. Limata, C. Mazzocchi, R. Menegazzo, P. Prati, V. Roca, C. Rolfs, M. Romano, C. R. Alvarez, E. Somorjai, O. Straniero, F. Strieder, F. Terrasi, H. P. Trautvetter, and A. Vomiero. Precision study of ground state capture in the 14N(p,γ)15O reaction. *Phys. Rev. C - Nucl. Phys.*, 78(2):1–4, 2008. ISSN 05562813. doi: 10.1103/PhysRevC.78.022802.

31. M. Marta, E. Trompler, D. Bemmerer, R. Beyer, C. Broggini, A. Caciolli, M. Erhard, Z. Fülöp, E. Grosse, G. Gyürky, R. Hannaske, A. R. Junghans, R. Menegazzo, C. Nair, R. Schwengner, T. Szücs, S. Vezzú, A. Wagner, and D. Yakorev. Resonance strengths in the N14(p,??)O15 and N15(p,????)C12 reactions. *Phys. Rev. C - Nucl. Phys.*, 81(5):1–10, 2010. ISSN 05562813. doi: 10.1103/PhysRevC.81.055807.

32. M. Marta, A. Formicola, D. Bemmerer, C. Broggini, A. Caciolli, P. Corvisiero, H. Costantini, Z. Elekes, Z. Fülöp, G. Gervino, A. Guglielmetti, C. Gustavino, G. Gyürky, G. Imbriani, M. Junker, A. Lemut, B. Limata, C. Mazzocchi, R. Menegazzo, P. Prati, V. Roca, C. Rolfs, C. Rossi Alvarez, E. Somorjai, O. Straniero, F. Strieder, F. Terrasi, H. P. Trautvetter, and A. Vomiero. The N14(p,γ)O15 reaction studied with a composite germanium detector. *Phys. Rev. C - Nucl. Phys.*, 83(4):1–10, 2011. ISSN 05562813. doi: 10.1103/PhysRevC.83.045804.

33. C. Michelagnoli. *The lifetime of the 6.79 MeV state in 15 O as a challenge for nuclear astrophysics and γ -ray spectroscopy: a new DSAM measurement with the AGATA Demonstrator array*. PhD thesis, Università degli Studi di Padova Dipartimento, 2013.

34. A. M. Mukhamedzhanov, P. Bém, B. A. Brown, V. Burjan, C. A. Gagliardi, V. Kroha, J. Novák, F. M. Nunes, Š. Piskoř, F. Pirlepesov, E. Šimečková, R. E. Tribble, and J. Vincour. Asymptotic normalization coefficients for 14N+p 15O and the astrophysical S factor for 14N(p,g)15O. *Phys. Rev. C*, 67(6):065804, 2003. ISSN 0556-2813. doi: 10.1103/PhysRevC.67.065804. URL `http://link.aps.org/doi/10.1103/PhysRevC.67.065804`.

35. C. Rolfs and W. S. Rodney. *Cauldrons in the Cosmos*. 2005.

36. R. C. Runkle, A. E. Champagne, C. Angulo, C. Fox, C. Iliadis, R. Longland, and J. Pollanen. Direct Measurement of the 14N(p,g)15O S Factor. *Phys. Rev. Lett.*, 94:082503, 2005. ISSN 0031-9007. doi: 10.1103/PhysRevLett.89.262501. URL `http://link.aps.org/doi/10.1103/PhysRevLett.89.262501`.

37. S. G. Ryan and A. J. Norton. *Stellar Evolution and Nuclear Synthesis*. 2010.

38. A. Schimpf. *GEANT4 Simulation of a Doppler Shift Attenuation Experiment*. PhD thesis, Technische Universitat Munchen, 2011.

39. U. Schröder, H. Becker, G. Bogaert, J. Görres, C. Rolfs, H. P. Trautvetter, R. Azuma, C. Campbell, J. King, and J. Vise. REACTION RATE OF 14N (p , y)“ O AND HYDROGEN BURNING IN MASSIVE STARS *. *Nucl. Phys. A*, 467:240–260, 1987.

40. D. Schürmann, R. Kunz, I. Lingner, C. Rolfs, F. Schümann, F. Strieder, and H. P. Trautvetter. Lifetime measurement of the 6792 keV state in O15, important for the astrophysical S factor extrapolation in N14(p,g)O15. *Phys. Rev. C - Nucl. Phys.*, 77(5):1–7, 2008. ISSN 05562813. doi: 10.1103/PhysRevC.77.055803.

41. A. Serenelli, C. Peña-Garay, and W. C. Haxton. Using the standard solar model to constrain solar composition and nuclear reaction S factors. *Phys. Rev. D - Part. Fields, Gravit. Cosmol.*, 87(4):1–9, 2013. ISSN 15507998. doi: 10.1103/PhysRevD.87.043001.

42. A. M. Serenelli, S. Basu, J. W. Ferguson, and M. Asplund. NEW SOLAR COMPOSITION : THE PROBLEM WITH SOLAR MODELS REVISITED. *Astrophys. J.*, 705, 2009. doi: 10.1088/0004-637X/705/2/L123.

43. T. Szücs, D. Bemmerer, A. Caciolli, Z. Fülöp, R. Massarczyk, C. Michelagnoli, T. P. Reinhardt, R. Schwengner, M. P. Takács, C. A. Ur, A. Wagner, and L. Wagner. Determination of g-ray widths in 15N using nuclear resonance fluorescence. *Phys. Rev. C*, 92(1):014315, 2015. ISSN 0556-2813. doi: 10.1103/PhysRevC.92.014315. URL `http://link.aps.org/doi/10.1103/PhysRevC.92.014315`.

44. M. Turner. *Connecting Quarks with the Cosmos: Eleven Science Questions for the New Century*. 2003. ISBN 978-0-309-07406-3. URL `http://www.nap.edu/catalog.php?record{_}id=10079`.

45. L. Wagner, S. Akhmadaliev, M. Anders, D. Bemmerer, A. Caciolli, S. Gohl, M. Grieger, A. Junghans, M. Marta, F. Munnik, T. P. Reinhardt, S. Reinicke, M. Röder, K. Schmidt, R. Schwengner, M. Serfling, M. P. Takács, T. Szücs, A. Vomiero, A. Wagner, and K. Zuber. Astrophysical S factor of the N 14 (p,γ) O 15 reaction at 0.4-1.3 MeV. *Phys. Rev. C*, 97(1):1–15, 2018. ISSN 24699993. doi: 10.1103/PhysRevC.97.015801.

46. K. Yamada, T. Motobayashi, H. Akiyoshi, N. Aoi, Z. Fülöp, T. Gomi, Y. Higurashi, N. Imai, N. Iwasa, H. Iwasaki, Y. Iwata, H. Kobayashi, M. Kurokawa, Z. Liu, T. Minemura, S. Ozawa, H. Sakurai, M. Serata, S. Shimoura, S. Takeuchi, T. Teranishi, Y. Yanagisawa, K. Yoshida, and M. Ishihara. E1 strength of the subthreshold 3/2+ state in 15O studied by Coulomb

excitation. *Phys. Lett. Sect. B Nucl. Elem. Part. High-Energy Phys.*, 579(3-4):265–270, 2004. ISSN 03702693. doi: 10.1016/j.physletb.2003.11.024. URL http://dx.doi.org/10.1016/j.physletb.2003.11.024.